

A Measurement of the Temperature-Density Relation in the Intergalactic Medium Using a New Ly α Absorption Line Fitting Method ¹

Patrick McDonald,^{2,3} Jordi Miralda-Escudé,^{3,4} Michael Rauch,⁵ Wallace L. W. Sargent,⁶ Tom A. Barlow,⁶ and Renyue Cen⁷

ABSTRACT

The evolution of the temperature in the intergalactic medium is related to the reionization of hydrogen and helium, and has important consequences for our understanding of the Ly α forest and of galaxy formation in gravitational models of large-scale structure. We measure the temperature-density relation of intergalactic gas from Ly α forest observations of eight quasar spectra with high resolution and signal-to-noise ratio, using a new line fitting technique to obtain a lower cutoff of the distribution of line widths from which the temperature is derived. We carefully test the accuracy of this technique to recover the gas temperature with a hydrodynamic simulation. The temperature at redshift $\bar{z} = (3.9, 3.0, 2.4)$ is best determined at densities slightly above the mean: $T_{\star} = (20200 \pm 2700, 20200 \pm 1300, 22600 \pm 1900)$ K (statistical error bars) for gas density (in units of the mean density) $\Delta_{\star} = (1.42 \pm 0.08, 1.37 \pm 0.11, 1.66 \pm 0.11)$. The power-law index of the temperature-density relation, defined by $T = T_{\star}(\Delta_g/\Delta_{\star})^{\gamma-1}$, is $\gamma - 1 = (0.43 \pm 0.45, 0.29 \pm 0.30, 0.52 \pm 0.14)$ for the same three redshifts. The temperature at the fixed over-density $\Delta = 1.4$ is $T_{1.4} = (20100 \pm 2800, 20300 \pm 1400, 20700 \pm 1900)$ K. These temperatures are higher than expected for photoionized gas in ionization equilibrium with a cosmic background, and can be explained by a gradual additional heating due to on-going He II reionization. The measurement of the temperature reduces one source of uncertainty in the lower limit to the baryon density implied by the observed mean flux decrement. We find that the temperature cannot be reliably measured for under-dense gas, because the velocities due to expansion always dominate the widths of the corresponding weak lines.

¹The observations were made at the W.M. Keck Observatory, which is operated as a scientific partnership between the California Institute of Technology and the University of California; it was made possible by the generous support of the W.M. Keck Foundation.

²Department of Physics and Astronomy, University of Pennsylvania, Philadelphia, PA 19104

³Department of Astronomy, The Ohio State University, Columbus, OH 43210; mcdonald,jordi@astronomy.ohio-state.edu

⁴Alfred P. Sloan Fellow

⁵ESO, Karl-Schwarzschild-Str. 2, 85748 Garching, Germany

⁶Astronomy Department, California Institute of Technology, Pasadena, CA 91125

⁷Princeton University Observatory, Peyton Hall, Princeton, NJ 08544

Subject headings: cosmology: observations—intergalactic medium—quasars: absorption lines

1. INTRODUCTION

The Lyman- α forest absorption in the spectra of quasars provides a wealth of information about the properties of the intergalactic medium (hereafter, IGM). There has recently been a lot of interest in using the distribution of Doppler parameters of fitted absorption lines, measuring the total velocity dispersion of the gas, to constrain the temperature of the IGM (Schaye et al. 1999; Ricotti, Gnedin, & Shull 2000; Bryan & Machacek 2000). In this paper we develop a method to identify and to fit absorption lines, and to obtain the gas temperature from the distribution of the Doppler parameters of the lines. Our algorithm is intended to be simple to implement and be applied identically on simulations and observations.

The temperature of the IGM as a function of density is primarily determined by the balance between adiabatic cooling and photoionization heating, once ionization equilibrium with the background radiation has been established. However, during the epoch of reionization, the heating rate is higher because every atom needs to be ionized once (and the ionization can occur on a short time-scale compared to the recombination rate), and the high opacity of the low-density IGM implies that high-frequency photons are absorbed, delivering a much greater amount of heat for each ionization (e.g., Miralda-Escudé & Rees 1994; Hui & Gnedin 1997; Haehnelt & Steinmetz 1998; Abel & Haehnelt 1999; Gnedin 2000). Other sources of heating may also contribute, such as Compton heating by the X-ray background (Madau & Efstathiou 1999), or photoelectric heating by dust grains (Nath, Sethi, & Shchekinov 1999). Constraining these sources of heating is one of the two primary reasons why we are interested in measuring the temperature. The other reason is the need to make accurate predictions for the statistics of the Ly α forest flux in order to constrain cosmological parameters (e.g., Rauch et al. 1997; Weinberg et al. 1997; Croft et al. 1998; Hui 1999; McDonald & Miralda-Escudé 1999; Hui, Stebbins, & Burles 1999; Croft et al. 1999b; Weinberg et al. 1999; Croft, Hu, & Davé 1999a; Nusser & Haehnelt 2000; McDonald et al. 2000). The temperature-density relation affects the predicted relationship between the power spectrum of the transmitted flux and the power spectrum of the initial mass density perturbations (Nusser & Haehnelt 2000), as well as the predicted mean transmitted flux (Rauch et al. 1997; McDonald et al. 2000), which can be used to constrain the baryon density of the universe.

Recent Ly α forest simulations have shown that, when the structure of the absorption systems is adequately resolved, the predicted absorption line widths are smaller than observed if the temperature of the IGM is determined from photoionization equilibrium, well after reionization has ended (Theuns et al. 1998, 1999a; Bryan et al. 1999). To solve the discrepancy the temperature apparently needs to be higher. Several authors have presented measurements of the IGM temperature using different methods, generally finding values moderately higher than expected from photoionization equilibrium (Theuns et al. 1999b; Ricotti et al. 2000; Bryan & Machacek 2000;

Schaye et al. 2000).

Our aim in this paper is to provide a new unambiguous measurement of the temperature, making a more exhaustive analysis than in previous work of the model uncertainties that result from comparing the observational results with a simulation. We develop a new line-fitting method as an alternative to the standard Voigt-profile fitting with line deblending, which is much faster, unambiguous, and easy to implement. Our method works by essentially assigning one line to each sufficiently deep minimum in the transmitted flux, and measuring the line width and central optical depth for each line. The gas temperature at each density is then derived from the distribution of line widths at each central optical depth. The systematic uncertainties and model dependence of the method used to derive the temperature are carefully analyzed, in a more extensive way than it was done in previous work. The new method is applied to observational data and to a simulation in exactly the same way, computing error bars due to the variance in our observed sample.

The main idea of the method to measure the temperature of the IGM was suggested by Schaye et al. (1999), Ricotti et al. (2000), and Bryan & Machacek (2000). The probability distribution of Doppler parameters, $P(B)$, is characterized by a lower cutoff, B_C , where $P(B)$ rises sharply, with very few lines having narrower Doppler parameters than this cutoff. The idea is that this cutoff is a measure of the gas temperature. In general, absorption lines have both a thermal and a hydrodynamical contribution to their breadth; however, for any set of lines with similar gas temperature, the narrowest ones will be those where the velocity field along the line of sight through the absorber is close to a caustic, so that the variation in the fluid velocity is minimized and thermal broadening dominates the observed line width. In fact, it was found by Theuns et al. (1999b) that the narrowest absorption lines are primarily thermally broadened.

A tight relationship between density and temperature in the IGM for gas at low densities, where shock heating is not very important, is expected theoretically and is found in numerical simulations (Hui & Gnedin 1997; Theuns et al. 1998). This implies that the narrowest lines at a given gas density (corresponding approximately to the optical depth at the line center) are not selected to have low gas temperature, but low fluid velocity dispersion. This justifies estimating the temperature from the lower cutoff of the Doppler parameter distribution.

In §2 we briefly describe the observational data and the simulation that we use. In §3 we describe our line fitting algorithm. In §4 we demonstrate how the line fitter works by running it on spectra from the numerical simulation. In §5 we describe our method for estimating the temperature from Doppler parameter distribution, testing the conditions under which the temperature can be recovered in a model-independent way. In §6 we use the line fitter on the observational data and give results for the measured temperatures. The results are discussed in §7. The Appendix describes further details of our line-fitting method.

2. THE OBSERVATIONAL DATA AND THE SIMULATION

2.1. Observations

We use the same set of eight quasar spectra as in Paper I. These spectra have sufficiently high resolution and signal-to-noise ratio to measure the shape of each absorption feature. The pixel noise is typically less than 5% of the continuum flux level, and frequently as low as 1%. The velocity resolution is 6.6 km s^{-1} (FWHM) and the spectra are binned in 0.04 \AA pixels. More details and statistics of this data set are given in Paper I and references therein.

The seven quasars from the Rauch et al. (1997) data set have previously constructed lists of regions that are suspected of containing metal lines. Our main results include these regions in the spectra because they are not positively identified as containing metal lines.

In Paper I we defined three redshift bins: $3.39 < z < 4.43$, $2.67 < z < 3.39$, and $2.09 < z < 2.67$, with mean redshifts $\bar{z} = 3.9$, $\bar{z} = 3.0$, and $\bar{z} = 2.4$. We use these same three bins in this paper, which contain approximately the same amount of data.

2.2. Simulation

We test the profile fitting code and the procedure to measure the temperature on the output of the Eulerian hydrodynamical simulation described in Miralda-Escudé et al. (1996) (referred to as L10 in that paper). The cosmological model used has $\Omega_0 = 0.4$, $\Omega_\Lambda = 0.6$, $h = 0.65$, $\sigma_8 = 0.79$, and large scale primordial power spectrum slope $n = 0.95$. The box size of the simulation is $10h^{-1}$ Mpc, and it contains 288^3 cells. We use outputs from the simulation at $z = 4, 3$, and 2 .

2.2.1. Generation of Simulated Spectra

$\text{Ly}\alpha$ spectra are computed for a large number of lines of sight along the box axes. There is one free parameter that we can vary when computing the spectra, the normalization of the optical depth, which we adjust to reproduce the mean transmitted flux of the observations that we are comparing to (the values of the mean transmitted flux are taken from Paper I). Renormalizing the optical depth is equivalent to modifying the intensity of the ionizing background, as long as the effect of collisional ionization and the change in the gas temperature caused by the different heating rate can be neglected (see Theuns et al. 1998 for a test that these effects are in fact negligible). The optical depth is then mapped to transmitted flux using $F = \exp(-\tau)$.

For each line of sight through the simulation (parallel to one of the three axes), we estimate the effects of continuum fitting by defining the maximum transmitted flux along the line of sight to be the continuum flux, F_c , and dividing the flux in all other pixels in the line by F_c . We map the 288 cells along a line of sight onto smaller cells, with their size chosen to match the observations

that we want to compare to. Finally we convolve the spectra with the instrumental resolution of 6.6 km s^{-1} , and we add Gaussian noise to each cell with a flux dependent dispersion $n(F)$, which is taken from Paper I.

2.2.2. The $T - \Delta_g$ Relation in the Simulation

Before we describe the method we shall use to measure the temperature, it will be useful to examine the temperature-density relation in the simulation. In this paper we parameterize the mean temperature-density relation (hereafter referred to as the $T - \Delta_g$ relation) as a power-law, $T = T_0 \Delta_g^{\gamma-1}$, where the gas over-density is $\Delta_g \equiv \rho_g / \bar{\rho}_g$, for the purpose of measuring this relation from the data. Although the $T - \Delta_g$ relation naturally approaches a power-law form with $\gamma - 1 \simeq 0.6$ when the thermal evolution is determined by photoionization heating and adiabatic expansion alone (Hui & Gnedin 1997), in general it deviates significantly from a power-law. Figure 1 shows scatter plots of T versus Δ_g for the three redshift outputs of the simulation. The solid lines are power-law fits to the range $1 < \Delta_g < 2$, to show that the $T - \Delta_g$ relation in the simulation is only roughly consistent with a power law. There is a substantial dispersion of the temperature at a given density, and the relation between the mean temperature and the density deviates from a power-law. For example, using the $z = 3$ simulation output, the best power-law fits in the restricted ranges of density $\Delta_g = (0-1, 1-2, 2-3)$ yield $\gamma - 1 = (0.15, 0.30, 0.39)$, with a mean fractional temperature deviation around the fits equal to (4%, 11%, 18%). The dispersion is due to shock-heating and to the variable expansion or contraction histories of the gas at a fixed density. The reionization of He II occurs near $z \sim 3$ in this simulation, heating the low-density gas to a temperature that is nearly constant with density. The parameters of the power-law fits to all three simulation outputs, in the range $\Delta_g = (1-2)$, are given in Table 1.

Because of this deviation from a power-law form of the $T - \Delta_g$ relation, a measurement of the temperature T_0 and power-law index γ should be understood only as an approximation to the true mean $T - \Delta_g$ relation, near the effective density at which the measurement is made, and this effective density needs to be specified. We use the following form to present our results in §6:

$$T = T_\star (\Delta_g / \Delta_\star)^{\gamma-1}, \quad (1)$$

where Δ_\star is chosen so that the error bars on T_\star and $\gamma - 1$ are uncorrelated.

2.2.3. Definition of Temperature and Density at Points in Spectra

Each pixel in a spectrum receives optical depth contributions from an extended stretch of real space along the line of sight, so no unique temperature or density can be associated with the pixel. However, we can define the temperature and the gas density at pixels in spectra to be the optical depth-weighted average over the temperature and the density of all the gas that

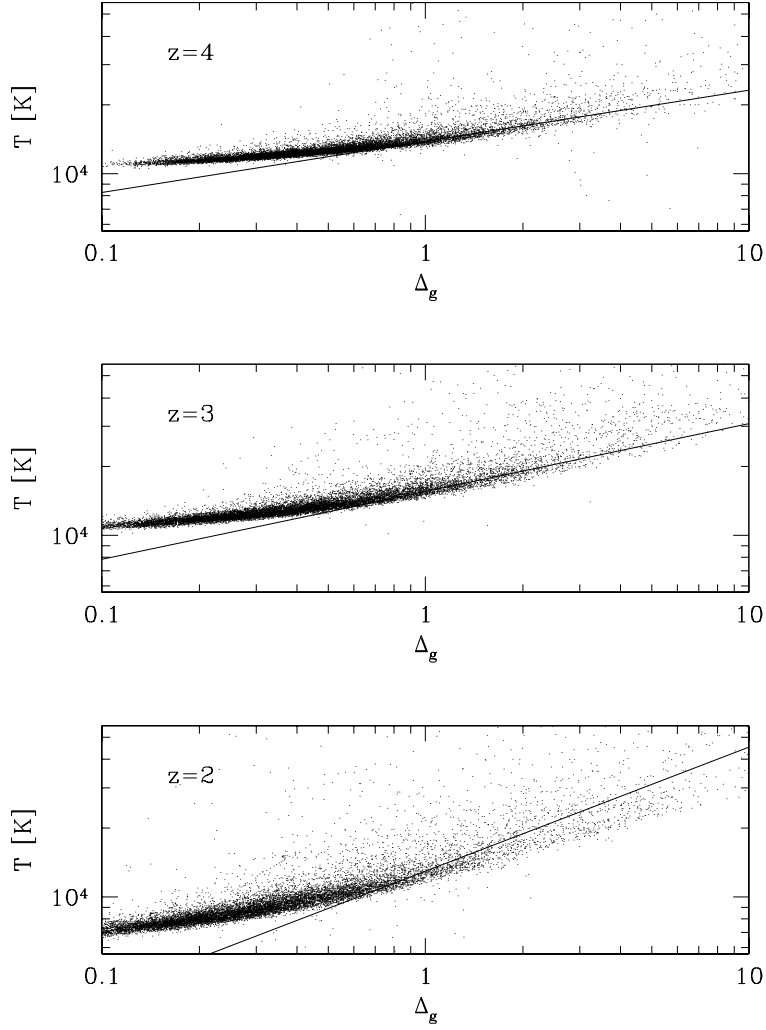


Fig. 1.— Temperature vs. density for random points in real space from the simulation. The lines are minimum absolute deviation power-law fits to each set of points in the restricted range $1 < \Delta_g < 2$; the fitted parameters are given in Table 1.

contributes to absorption in the pixel. This definition will be used later to assign a gas temperature to any identified absorption line, which we will define to be equal to the temperature of the central pixel. Table 1 shows fits to the $T - \Delta_g$ relation for pixels, restricted over the same density range $1 < \Delta_g < 2$: we see that the mean relation is almost the same as for random points in space. This is true in spite of a larger difference in the density distribution; for example, the median Δ_g is $(0.47, 0.39, 0.31)$ for random points at $z = (4, 3, 2)$, and is $(0.52, 0.47, 0.41)$ for spectral pixels. This difference in the median density is caused by the thermal broadening and velocity dispersion in absorbers, which spread high density regions out into low density regions.

3. FITTING METHOD

In this section we describe the procedure that we use to identify and fit absorption lines. The temperature measurement is based on the identification of absorption lines that can be adequately fit by a single Gaussian in optical depth, over a certain interval around a point where the optical depth is maximum; the narrowest widths among the lines that can be fitted in this way will give us the gas temperature. Absorption systems that cannot be fitted by a single Gaussian must be broadened by a non-Gaussian distribution of the fluid velocity, and can therefore be discarded for the purpose of measuring the gas temperature. In contrast to the standard Voigt profile fitting approach, we make no attempt to fit the entire spectrum by superposing many absorption lines. Instead, we fit only small regions around minima of the transmitted flux, each one with a single Gaussian absorber. We therefore have a constant number of parameters to fit for each absorption line, making the algorithm simple, unambiguous, and fast.

Before we explain the procedure for identifying and fitting lines, it is useful to understand qualitatively what the results will look like. Figure 2 shows a section of the spectrum of Q1422, with the transmitted flux indicated by the dotted line, and the fitting solutions indicated by the solid lines. Our method has selected all statistically significant maxima in optical depth that are well fitted by a single Gaussian and identified them as absorption lines and has discarded the rest. The fits are done over the regions indicated by the solid lines. We will return to this figure once we have described the process used to fit the lines.

Our fitting method consists of taking each pixel in the spectrum as a candidate for containing the center of an absorption line. After requiring several conditions and eliminating most of the pixels as candidates, a final list of absorption lines is obtained, each one having a fitting window where a fit to the three parameters of the line (line center, central optical depth, and line width) is performed. None of the fitting windows from adjacent lines can overlap in the final list, as seen in the example of Figure 2.

The first operation is to determine an integer window width, W , which sets the fitting region around each pixel P , going from $P - W$ to $P + W$. The width W is the smallest one for which the following condition is obeyed, which ensures that there is a significant decline of the flux from the

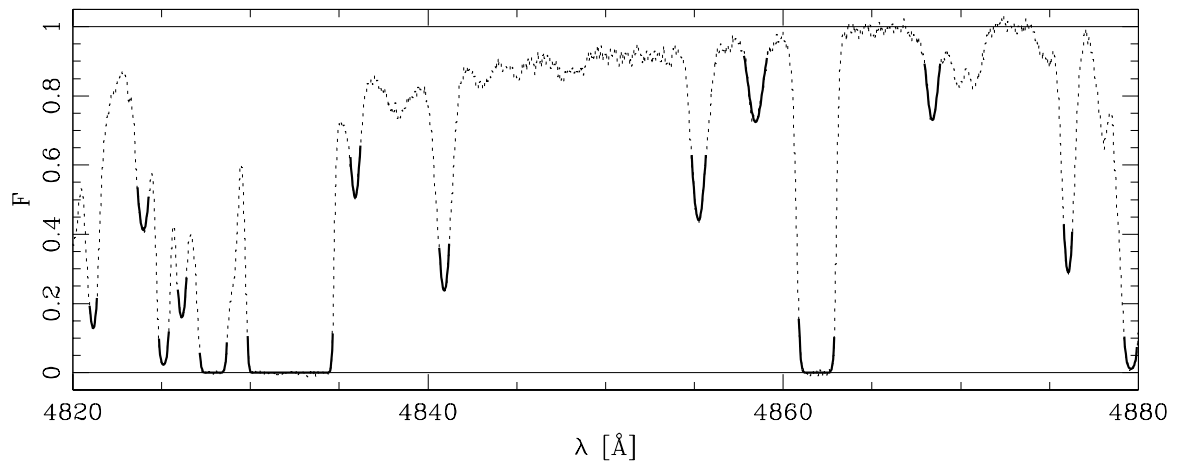


Fig. 2.— The dotted line shows a piece of an observed spectrum. The solid lines show the fitting results.

average value at the edges of the fitting window to the line center:

$$\frac{1}{2} [F(P+W) + F(P-W)] - F(P) > E_d \sigma(P, P \pm W) , \quad (2)$$

where

$$\sigma(P, P \pm W) \equiv \left[\sigma^2(P) + \frac{1}{4} (\sigma^2(P+W) + \sigma^2(P-W)) \right]^{1/2} , \quad (3)$$

$\sigma(P)$ is the noise at pixel P , and E_d is the first parameter of the fitting algorithm. E_d is the number of “ σ ” significance required of the flux decrease.

There are of course some pixels where the condition in equation (2) is never obeyed for any width. In practice, the width W is increased only up to some maximum value W_{max} before the pixel is discarded as a candidate for a line center. This maximum width is chosen to be large enough so that it does not affect the results of the algorithm. In addition, the minimum value of W is set to 2 pixels (so that the fitting region has at least 5 pixels). Some additional parameters are used in the algorithm to expedite the elimination of pixels as candidates for line fits, increasing the speed of the code without affecting the final result; these details are described in the Appendix.

For each pixel P where a fitting width W has been determined in this way, the line fit is performed by χ^2 minimization. We fit the following profile to the flux within the window:

$$F(v) = \exp \left[-\tau_c \exp \left(-\frac{1}{2} \frac{(v - v_c)^2}{\sigma_b^2} \right) \right] . \quad (4)$$

Here, v is the distance from the central pixel P . The three parameters of the fit are τ_c (the optical depth at the line center), v_c (the location of the line center), and σ_b (the width of the line). The parameter v_c is constrained to lie within the pixel P , so that when P is not close to the center of the line, a good fit will not be obtained. To account for the instrumental resolution, the function in equation (4) is convolved with a Gaussian filter of width matching the resolution of the data. After the fit is performed, we impose a goodness-of-fit requirement: the probability of exceeding by chance the value of χ^2 for the best fit should be larger than a certain value P_0 , which is a second parameter of our method. If the requirement is not satisfied, the pixel P is discarded as a candidate for including the center of an absorption line. The two parameters E_d and P_0 can be adjusted to optimize the temperature measurement, based on tests using numerical simulations that we will present in §4.

Because we require v_c to be within pixel P , acceptable fits to absorption lines are only found in pixels that are indeed close to a minimum of the flux, in an absorption feature that can be adequately fitted to a single Gaussian within a certain window. Typically, the list of pixels where acceptable fits are found will include groups of a few adjacent pixels around such minima. The final step of our algorithm is to select among any group of pixels with accepted line fits that are within their own fitting windows the one that yielded the best fit. This produces the final list of absorption lines.

We can now understand the fitting example shown in Figure 2. The widths of the fitting windows, shown by the solid lines, are set by the value of E_d (here, $E_d = 12$) and the noise level (which in this case varies from ~ 0.004 in saturated pixels to ~ 0.01 at the continuum). The apparent maxima of absorption that have no corresponding fitted line do not increase in flux enough at their edges to satisfy the requirement in equation (2). The cluster of fitted lines near $\lambda = 4830\text{\AA}$ demonstrates that our procedure does not automatically eliminate lines in blends, as long as they are clearly distinct maxima. Apparently, the requirement that the optical depth be consistent with a Gaussian curve is easily fulfilled by the peaks of all of the significant absorption lines.

Throughout this paper, we shall be expressing all results concerning the line widths in terms of the equivalent temperature, denoted as B , when the line width is assumed to be due to thermal broadening: $B \equiv 10000 (\sigma_b/9.09 \text{ km s}^{-1})^2 \text{ K}$. This allows for an easier comparison of the results of numerical simulations and observations. Note that line widths have usually been presented in the literature in terms of the Doppler parameter, $b = 2^{1/2}\sigma_b$.

An important property of this algorithm is that the distribution of line widths it measures should converge to a fixed answer as the signal-to-noise ratio of the observations is increased. In the limit of negligible noise and pixel size, and perfect resolution, every true minimum of the transmitted flux in the spectrum should be identified, and the fitted line width should reflect the second derivative around the minimum, because the size of the fitting window around each minimum should be very small. Moreover, the second derivative around minima is a physically well motivated quantity to obtain the gas temperature. In contrast, the Voigt profile fitting method does not converge at high signal-to-noise ratio because the number of blends assumed in an absorption system will change. Whereas the Voigt profile method attempts to fit the entire spectrum by superposing lines, our new method fits only small regions around the minima of transmitted flux as arising from a single absorber.

4. APPLICATION OF THE PROFILE FITTER TO THE NUMERICAL SIMULATION

4.1. Detailed Example of Fitting the Simulated Spectra

We now apply our method to 1500 randomly selected lines of sight through the simulation output at $z = 3$, with the mean flux decrement, noise level and pixel size set to match the observations at $\bar{z} = 3$ (see Paper I). We first set the two parameters of the line-fitting algorithm to $E_d = 12$ and $P_0 = 0.01$ (we shall analyze the optimal values of these parameters in §4.2). A total of 6378 lines are identified and successfully fitted. For each absorption line we obtain four quantities: the optical depth at the line center, τ_c ; the Doppler parameter converted to temperature units, B ; the optical-depth-weighted temperature at the central pixel, T ; and the optical-depth-weighted gas density at the central pixel, Δ_g .

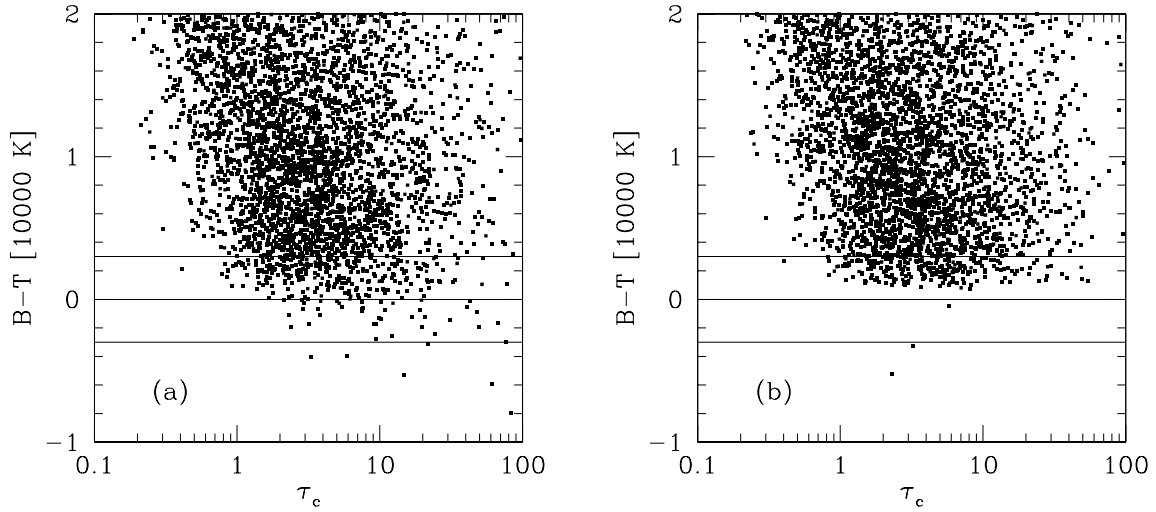


Fig. 3.— The difference, $B - T$, between the temperature estimated from the profile width and the true temperature at the profile center, plotted against the central optical depth τ_c , for absorption lines in the simulated spectra at $z = 3$. Noise at the same level as the observations at $\bar{z} = 3$ analyzed in §6 is included in (a), and not included in (b).

Figure 3(a) shows $B - T$ vs. τ_c for all 6378 fitted lines. The solid lines at $B - T = 0$ K and $B - T = \pm 3000$ K are to guide the eye in evaluating the contribution of non-thermal broadening to B . The noise that has been added to the simulated spectra (see §2.2.1) is responsible for most of the absorption lines with $B < T$. In Figure 3(b) we show the fitted lines from the same set of spectra as Figure 3(a), but without adding noise (although the noise level that each pixel should have been used to weight the χ^2 fits); the small number of lines that had $B < T$ in the presence of noise have been almost entirely eliminated (the few remaining lines with $B < T$ arise because the optical-depth-averaged temperature at the central pixel of a line can be skewed by a contribution from very hot gas).

Figure 3 demonstrates that the contribution to B from fluid motions is generally large, and therefore the Doppler parameter of an individual line will usually overestimate the gas temperature. For $\tau_c \gtrsim 1$, the distribution of $B - T$ extends to values as low as ~ 1000 K, implying that the lower cutoff in the B distribution should provide a good measure of the median gas temperature at a given τ_c [assuming that the lowest gas temperatures do not extend very much below the median value, as is true in the simulation (Fig. 1)]. However, for weak lines ($\tau_c < 1$), thermal broadening is never clearly dominating, preventing a model-independent estimate of the gas temperature at the correspondingly low gas densities. The reason why the breadth of weak lines is always dominated by motions is that all the low density gas has not turned around from the Hubble expansion.

The eight histograms in Figure 4, constructed from the same fitted lines as Figure 3(a), show more quantitatively the cutoff on the $B - T$ distribution near $B - T = 0$, for different optical depths. In the $\tau \sim 0.3$ and $\tau \sim 0.6$ panels of the Figure, the problem of estimating the temperature of the lower density gas is clearly seen. Over the range $1 \lesssim \tau \lesssim 20$, the distribution of $B - T$ is the desirable one for our temperature measurement: there are many lines near $B - T = 0$, but very few with $B < T$.

The sharpness of the cutoff in Figure 4 should of course be degraded in the observable B distribution, owing to the scatter in the temperatures of the lines. Figure 5 shows histograms of B along with histograms of T . By observing the histogram of B we would like to determine the median of T . For $\tau_c > 1$, the cutoff on the distribution of B appears to coincide well with the peak of the distribution of T . As we saw clearly in Figure 3, the number of lines with $B \simeq T$ decreases quickly for $\tau_c < 1$.

It is interesting to note in Figure 5 the change in the distribution of the true temperature in the simulation with τ_c . At low optical depth, the T distribution is very narrow as a result of the simplicity of the evolution history of gas at low density, which generally expands peacefully in the voids, heated by photoionization and cooled adiabatically by its expansion. As the density increases, the heating history of the gas becomes more heterogeneous. The gas at higher densities is shock-heated more frequently and to a greater degree, and the evolution of the density itself since reionization (when the initial temperature is set) is more highly variable. For $\tau \gtrsim 10$ the range of gas temperatures increases, making the interpretation of the cutoff on the B distribution more

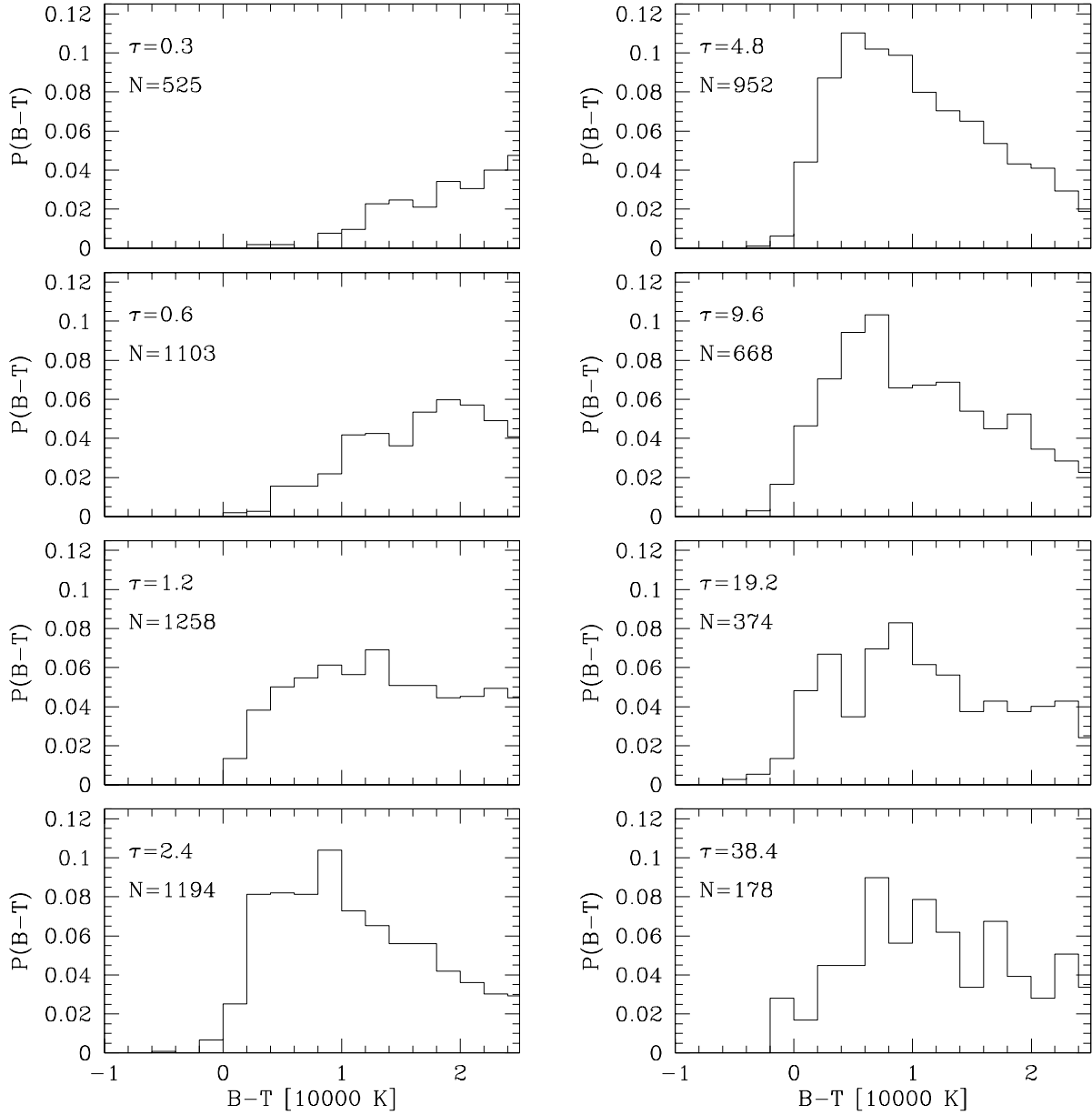


Fig. 4.— Distribution of the non-thermal broadening contribution to the line widths, $B - T$, at eight bins of the optical depth at the line center, τ_c . N is the total number of lines in each τ_c bin.

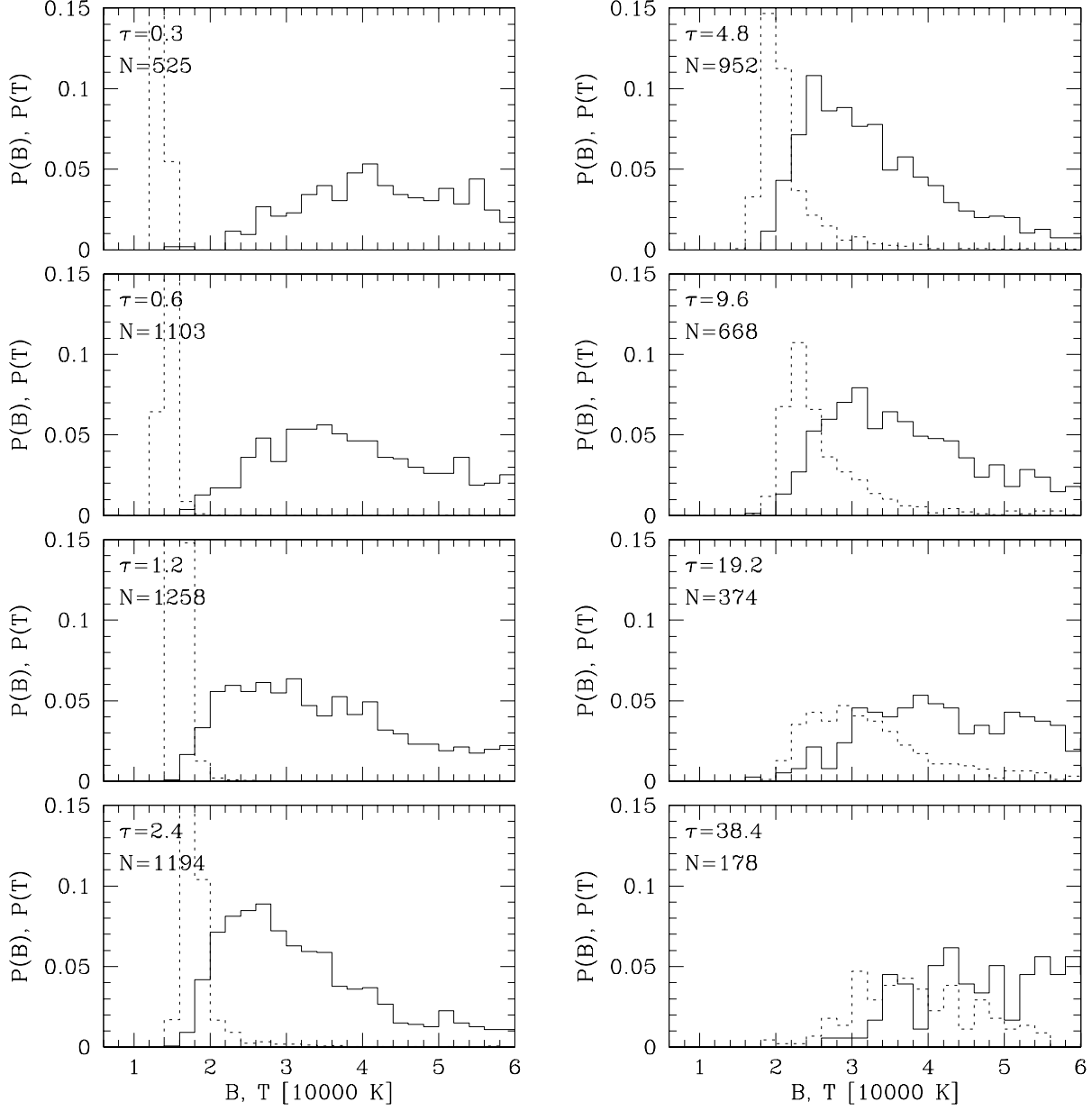


Fig. 5.— The solid lines show the histograms of B and the dotted lines show the histograms of T . The fitted lines used here are the same ones shown in the previous several Figures (described in §4.1). The probabilities in the T histograms are all reduced by a factor of 2.5 to facilitate visual comparisons.

ambiguous.

4.2. Optimizing the Fitting Control Parameters

The two parameters of the line fitter, E_d and P_0 , should be optimized to give the best statistical error bars on the location of the lower cutoff of the distribution of B , which we will use to estimate the gas temperature. In order to do this optimization, we define a quality measure, $Q = (N_g - N_b)(N_g + N_b)^{-1/2}$, where N_g and N_b are the number of fitted lines with $0 \text{ K} < B - T < 3000 \text{ K}$, and with $-3000 \text{ K} < B - T < 0 \text{ K}$, respectively. Basically, Q is a measure of the statistical significance of the increase in the number of lines as the $B = T$ cutoff is crossed, computed by comparing the number of lines in bins of width 3000K on each side of the cutoff. The larger the value of Q , the more accurately we should be able to determine the temperature. For example, the set of fitted lines shown in Figures 3-5 (fitted using $E_d = 12$ and $P_0 = 0.01$) gives $N_g = 281$ and $N_b = 40$, resulting in $Q = 13.5$. When we remove the noise in Figure 3(b) we find $N_g = 236$ and $N_b = 1$, yielding $Q = 15.3$. We use a bin width of 3000 K because the errors in the measured temperature from our data will be of about this magnitude (see §6).

Table 2 shows the Q values for a broad range of values of E_d , and $P_0 = 0.01$. We also list the Q value using two different values of P_0 , removing the noise from the spectra, removing the continuum fitting approximation, and using different random seeds for the added noise. We find that the changes in Q are usually smaller than the changes that can result from simply using a different set of random numbers for the noise that is added to the spectra. We conclude that the precise values taken by the parameters are not actually very important to the results. We use $E_d = 12$ and $P_0 = 0.01$ when we analyze spectra matching the $\bar{z} = 3$ observational properties in the rest of this paper. From the range of E_d with Q close to its maximum, we chose the smallest value of E_d , $E_d = 12$, because we expect that increasing the number of accepted lines will make the analysis procedure more robust, particularly the computation of the error bars.

We use two other redshift bins for the observational data (see §2.1), $\bar{z} = 2.4$ and $\bar{z} = 3.9$. Because the mean flux decrement, pixel size, and noise level are different in each bin, we determine a best value of E_d separately for each. Tests similar to the one in Table 2, using the mean flux decrement, noise level, and pixel size matching the observations in the high and low \bar{z} bins, show that $E_d = 9$ and $E_d = 8$ are the best values to use when analyzing data in the $\bar{z} = 2.4$ and $\bar{z} = 3.9$ bins, respectively, although the values of Q obtained are only weakly sensitive to E_d in each case. We fix $P_0 = 0.01$ at all three redshifts, because changing it does not significantly increase Q .

5. TESTS OF THE DERIVATION OF THE IGM TEMPERATURE USING THE SIMULATION

In this section we combine our line fitting method with elements of the method of Bryan & Machacek (2000) for constraining the temperature of the IGM by measuring the lower cutoff on the distribution of B . First we define the cutoff and how we associate it with an estimated temperature. Then we use the simulation to translate the observed temperature-optical depth relation into the desired $T - \Delta_g$ relation. All the results in this Section are obtained from the simulation. In §6 we present results for the temperature measured from the observational data, using the method described in this Section.

5.1. Locating the Cutoff on the Distribution of B

Bryan & Machacek (2000) presented a useful technique for quantifying the lower cutoff on a B histogram like those in Figure 5. They smooth the histogram with a Gaussian filter and define the cutoff to be the location of the maximum of the first derivative of the smoothed histogram. This derivative is given by

$$\frac{dP}{dB_i} \propto \sum_{j=1}^N (B_j - B_i) \exp \left[-\frac{1}{2} \frac{(B_i - B_j)^2}{\sigma_B^2} \right], \quad (5)$$

where the i th bin has temperature B_i , j is the label for N individual fitted absorption lines with fitted temperature B_j , and σ_B is the smoothing length. We plot in Figure 6 the smooth histogram of B and its derivative, as well as the smoothed histogram of the gas temperature, for $\sigma_B = 5000$ K, using spectra from the $z = 3$ simulation output with the $\bar{z} = 3$ observational noise, pixel size and mean flux decrement.

We define the Doppler parameter cutoff, $B_C(\tau_c)$, to be the value of B where dP/dB , given by equation (5), is maximum, for the optical depth bin labeled by τ_c . Our estimate of the gas temperature at optical depth τ_c is $B_C(\tau_c)$, after applying a small correction that we describe in detail in the remainder of this section.

5.1.1. Error Bars on $B_C(\tau_c)$

We compute error bars on the location of the cutoff on the B distribution (B_C) by bootstrap resampling (Press et al. 1992). We generate a bootstrap realization of the B histogram, for an optical depth bin containing N fitted lines, by selecting N lines at random from those in the bin (with replacement) and recomputing the histogram from the new set of lines. The error on B_C is given by the dispersion in the B_C values measured from many bootstrap realizations of the histogram.

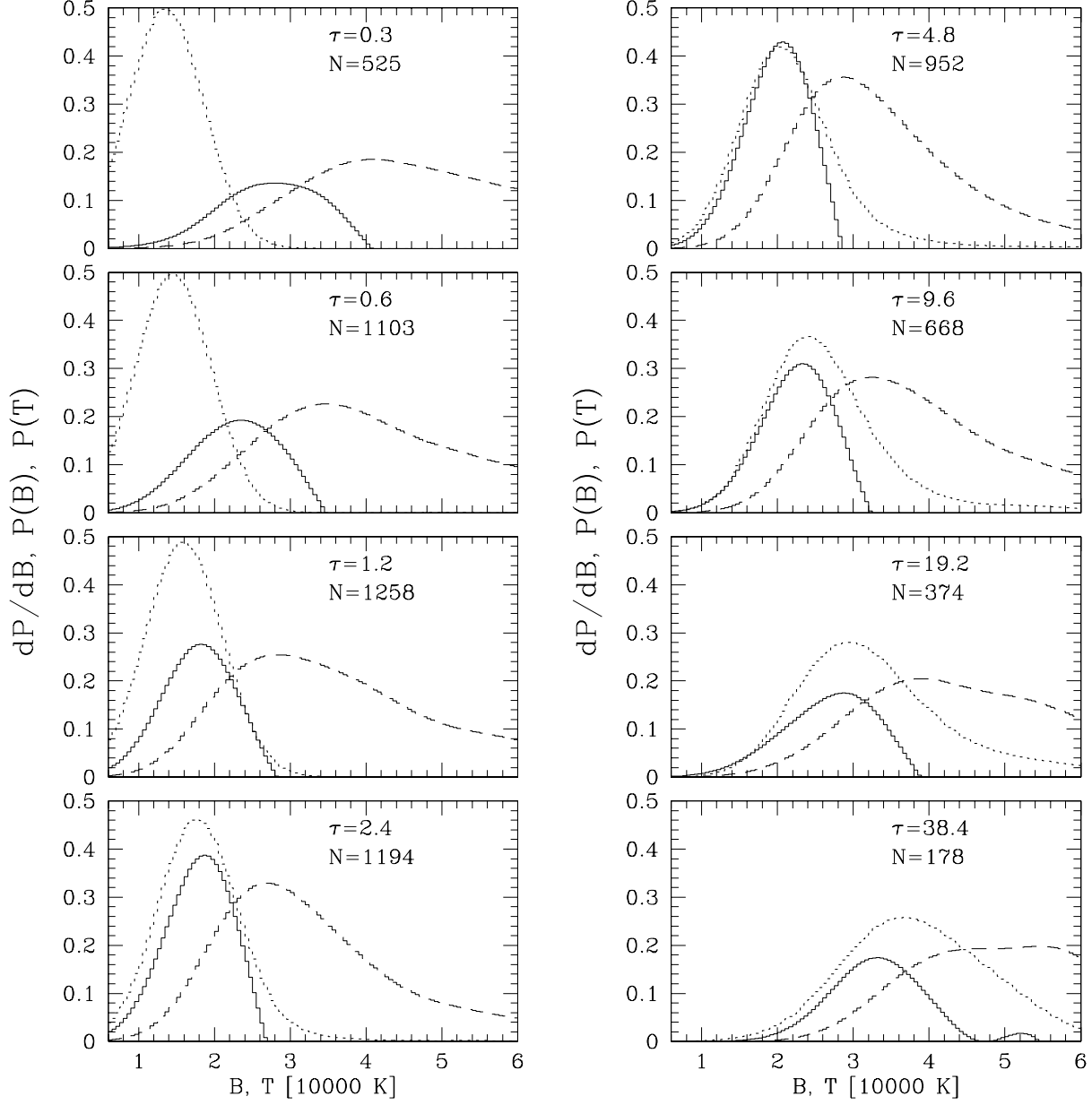


Fig. 6.— The derivative of the smoothed histogram of B (*solid line*), the smoothed histogram of B (*dashed line*), and the smoothed histogram of T (*dotted line*), from the absorption lines fitted in the $z = 3$ simulation output with the fitting control parameters $E_d = 12$ and $P_0 = 0.01$. The smoothing length is $\sigma_B = 5000$ K. The curves are arbitrarily normalized for clarity.

5.2. Comparison Between $B_C(\tau_c)$ and the Temperatures in the Simulation

In this subsection we investigate the relationship between $B_C(\tau_c)$ and the physical temperature, T , of the absorbers with central optical depth τ_c . We use spectra from the simulation, where we know the optical-depth-weighted temperature and density, T and Δ , of the absorption lines. We match the simulated spectra to the mean flux decrement, noise level and pixel size of the observations at $\bar{z} = 3$ (see §2.2.1). In §5.3 we show how the comparisons change when the simulated spectra are matched to the properties of the $\bar{z} = 3.9$ and $\bar{z} = 2.4$ observations.

Figure 7 explores the meaning of $B_C(\tau_c)$ in detail, using the $z = 3$ simulation results. We have separated all the fitted lines into 10 bins of the central optical depth, τ_c , choosing the bins so that each contains an equal number of absorption lines. We smooth the B histogram with $\sigma_B = 5000 \text{ km s}^{-1}$ to compute the cutoff temperature in every optical depth bin. Then, we compute the median central optical depth and gas temperature of the set of absorption lines that satisfy $|B - B_C| < 5000 \text{ K}$, in each optical depth bin. These sets of lines are the ones that actually determine the location of the cutoff in the B histogram, so we examine first the relation between B_C and their median temperature, which we denote by T_P . The values of B_C are shown as crosses with error bars.⁸ The temperature T_P is shown as the filled squares (the errors on the temperature are much smaller than those on B_C).

The triangles in Figure 7 show the effect on the derived cutoff, B_C , of reducing the histogram smoothing to $\sigma_B = 3000 \text{ K}$. There is no important difference with the crosses (the error bars for this smaller smoothing are similar to those on the crosses). By experimenting with different values of σ_B , we have found that B_C is not affected if σ_B is reduced, although the error bars obtained are significantly larger when reducing it below $\sigma_B = 3000 \text{ km s}^{-1}$. Increasing σ_B beyond 5000 km s^{-1} leads to an increase of B_C , because the smoothing is then larger than the intrinsic sharpness of the cutoff in the B distribution. We therefore adopt $\sigma_B = 5000 \text{ K}$ from this point forward in the paper.

The open squares show the effect of using *all* the absorption lines in every optical depth bin to compute the median temperature and optical depth, rather than using lines with $|B - B_C| < 5000 \text{ K}$ only. There is a negligible difference in the derived temperature of the absorbers as a function of τ_c ; the reason is that, as we have previously seen, broader lines are by and large systems with higher fluid velocity dispersions, but their gas temperatures are not significantly greater, except at the highest optical depths where there is a slight difference (the systematic shift to the right of the open squares relative to the filled ones is due to a larger median optical depth of the broad lines within each optical depth bin). In the rest of the paper, we always compute the medians of any properties of the absorption lines using only lines with $|B - B_C| < 5000 \text{ K}$.

⁸The error bars are from bootstrap realizations on 1500 lines of sight. In reality, these error bars may be slightly underestimated because the mean separation between 1500 lines of sight in the simulation we use is only $\sim 60 \text{ km s}^{-1}$, comparable to the flux correlation length in the spectra (Paper I). Obtaining better statistics of the theoretical prediction for B_C would require a larger simulation. However, for the analysis in the present paper the errors in the determination of the temperature from the observations are much larger.

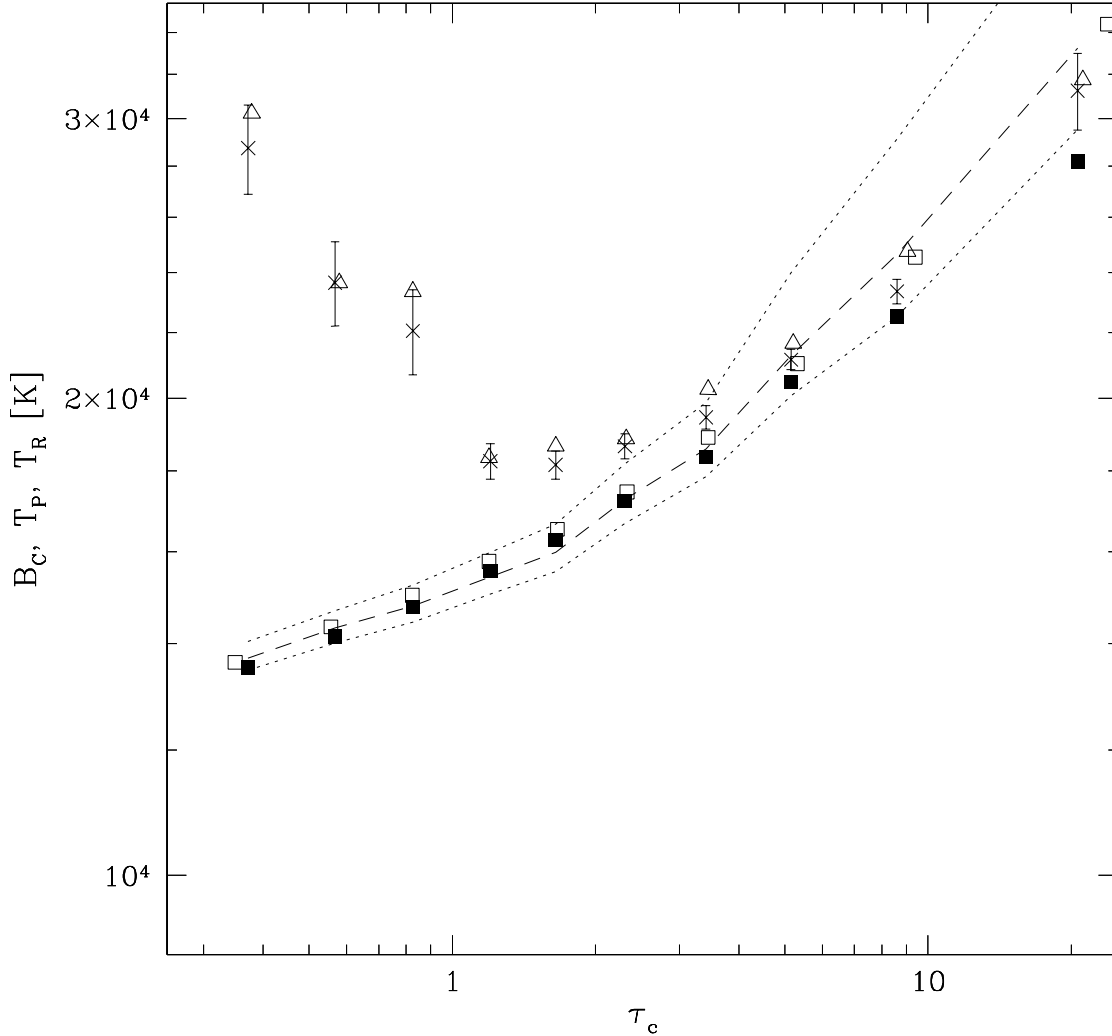


Fig. 7.— The crosses with error bars show $B_C(\tau_c)$, computed from the simulated spectra at $z = 3$, and using $\sigma_B = 5000 \text{ km s}^{-1}$. The open triangles show B_C when the smoothing of the B histogram is reduced to $\sigma_B = 3000 \text{ K}$. The open squares are the median T of all the absorption lines in each bin, while the filled squares are the median T of lines with $|B - B_C| < 5000 \text{ K}$ only. The dashed line shows T_R , the median value of T for random cells in the simulation, and the dotted lines show the 25th and 75th percentiles.

So far, we have seen that the Doppler parameter cutoff B_C provides a good estimator for the gas temperature of absorption systems at a given optical depth. Our ultimate goal, however, is to measure the median gas temperature at a given gas density, for randomly selected points in the IGM, which we shall henceforth refer to as T_R . The peaks in absorption are at special locations, so their median temperature, T_P , will generally not be exactly the same as T_R . To examine this question, we first compute the median density of the absorption lines in each optical depth bin, and then we calculate the median temperature of randomly selected points at this gas density. The result is shown as the dashed line in Figure 7; the dotted lines give the 25 and 75 percentiles of the temperature distribution at random points with the same gas density. Comparing the dashed line to the filled squares, we see that the fitted absorption lines with relatively large optical depth typically have $T_P < T_R$, i.e., they are colder than random fluid elements at the same density. We believe the reason for this effect is the characteristic double-shock structure around the absorbers (Cen et al. 1994): the gas in the highest density tube along a filament (or the highest density surface along a sheet) is located between shocks, so it has been subject to less shock-heating than the surrounding gas.

Our method of analysis of the observational data in §6 will automatically correct for this difference between the temperature of the absorption lines and the temperature at random points. This systematic difference may introduce a potential uncertainty in the derivation of the gas temperature if it depends on quantities like the resolution of the simulation, the cosmological model that is assumed, or the heating at the reionization epoch. However, the temperature difference between lines and random points is negligible compared to the observational errors we will compute for the temperature in §6, at least in the simulation we analyze here.

5.2.1. Testing With Other $T - \Delta_g$ Relations

We need to test the robustness of the finding that $B_C(\tau_c) \simeq T_P(\tau_c)$ for $\tau_c \gtrsim 1$, which we have established so far in tests on the $z = 3$ simulation output. We can change the $T - \Delta_g$ relation that we are measuring by simply using the $z = 2$ or $z = 4$ outputs from the simulation (see Table 1), still creating spectra with mean flux, noise level, and pixel size matching the $\bar{z} = 3$ observations, as described in §2.2.1. In addition to the varying $T - \Delta_g$ relations, these spectra have different amplitudes of fluctuations, and different Hubble constants.

Figure 8 shows the comparison between $B_C(\tau_c)$ and $T_P(\tau_c)$, using the $z = 2$ and $z = 4$ outputs of the simulation in addition to $z = 3$. The (*pentagons, squares, triangles*) show B_C for the $z = (4, 3, 2)$ simulation output, and the (*solid, long-dashed, short-dashed*) line show $T_P(\tau_c)$. We see that B_C traces the temperature changes at the different redshifts extremely well, tracking the different slopes at $z = 2$ and $z = 4$ perfectly, and matching the increased overall temperature at $z = 3$. All three redshift outputs show the same strong increase in B_C above the actual temperature for optical depths below unity, corresponding to $\Delta_g \sim 1$ in each case.

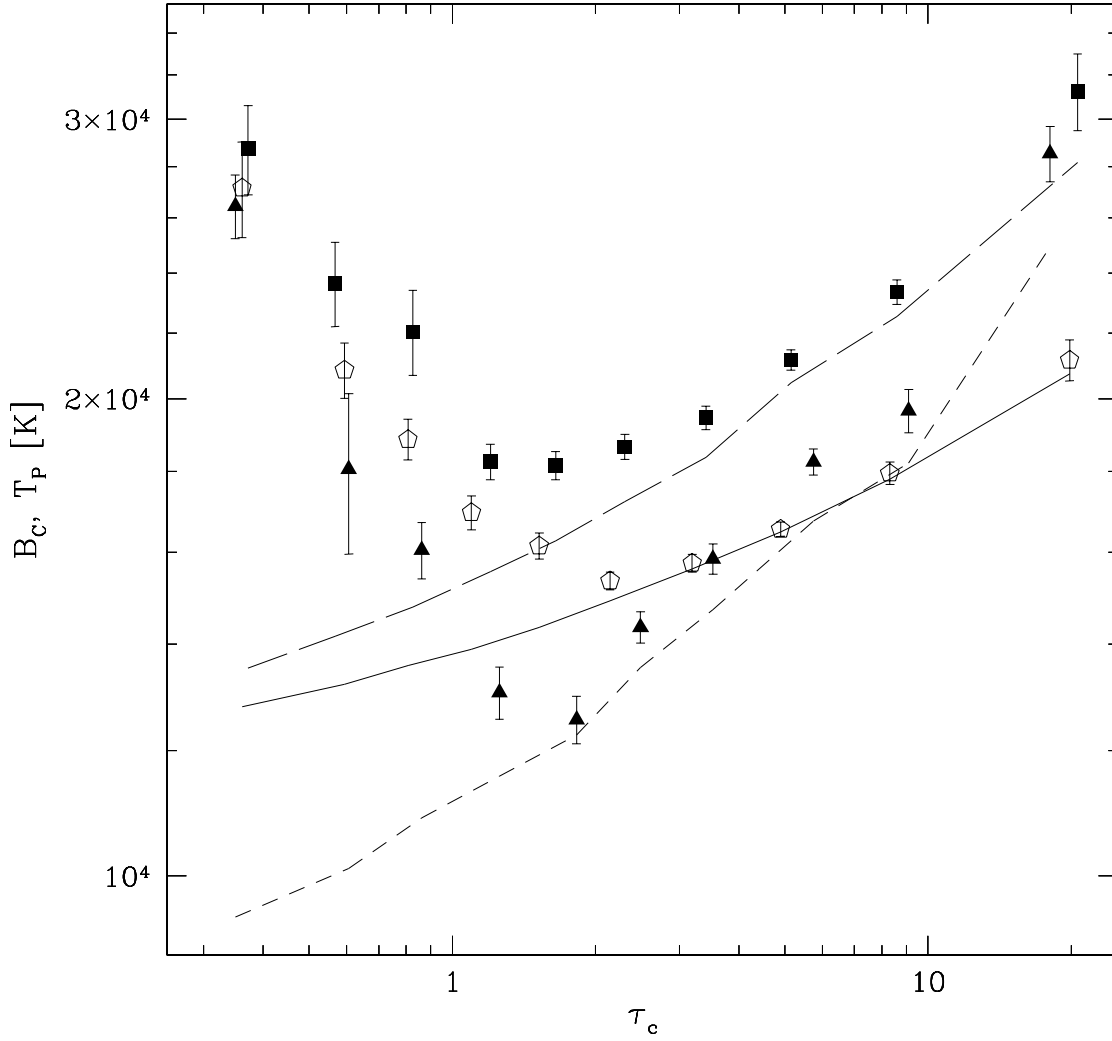


Fig. 8.— (*Pentagons, squares, triangles*): B_C for the $z = (4, 3, 2)$ simulation output. (*Solid, long-dashed, short-dashed*) lines: T_P (median temperature of fitted lines) for $z = (4, 3, 2)$. All simulated spectra have the mean flux decrement, pixel size and noise level set to match the $\bar{z} = 3.0$ observations.

5.3. The $B_C - T$ Relation at Different Redshifts

We have seen that B_C traces T_P remarkably well for the mean flux decrement and noise level of our observational data at $\bar{z} = 3$. We shall now verify that this is also true when the flux decrement and noise is set to the values appropriate for the other two redshift bins in which we separate the data, at $\bar{z} = 2.41$ and $\bar{z} = 3.89$.

We first introduce a new type of figure that shows more clearly how accurately $B_C(\tau_c)$ traces the gas temperature. Figure 9(a) shows $B_C - T_R$, where T_R is the median temperature of random points at the density of each optical depth bin (recall that this density is defined as the median density of absorption lines in each optical depth bin that have $|B - B_C| < 5000\text{K}$). The (*pentagons, squares, triangles*) are obtained from the simulation outputs at $z = (4, 3, 2)$, and are the same points as in Figure 8 except that we have subtracted T_R . The temperature is correctly traced by B_C at $\tau_c \gtrsim 1$, and drops below B_C at lower optical depths in the same way, independently of which simulation output we use. At $\tau_c > 10$, B_C falls significantly below the temperature in the $z = 2$ output (this is seen clearly using more optical depth bins). The reason is that the temperature dispersion is higher at $z = 2$ in the simulation, causing B_C to reflect the lower cutoff of the true temperature distribution.

The results when we fix the mean flux decrement and noise to the $\bar{z} = 2.41$ redshift bin of the observational data (taken from Paper I) are shown in Figure 9(b). Here, we use the parameters $E_d = 9$ and $P_0 = 0.01$ for the line fitting algorithm (see §3). The results are shown also using all three simulation outputs. Again, we find the temperature is well traced by B_C , but over a range of τ_c that has shifted to lower values. This is a result of the decreased optical depth at fixed gas density. Absorption systems that are primarily thermally broadened exist above a gas density that is approximately constant at each redshift, but the corresponding optical depth varies rapidly with redshift. At high optical depths, an additional effect is important in changing the degree to which B_C traces the gas temperature: the increased shock-heating at low redshifts (with increasing velocities of collapse) implies a higher temperature dispersion, even at a fixed gas density. Therefore, B_C drops further below the median gas temperature as the redshift decreases.

The result for $\bar{z} = 3.9$ is shown in Figure 9(c) (we use $E_d = 8$ at this redshift). The Doppler parameter cutoff (B_C) now traces the temperature only at high optical depth, $\tau_c \gtrsim 5$, for exactly the same reason: a fixed gas density has shifted to a significantly higher optical depth due to the increase in the mean flux decrement.

5.4. Determining $T_R(\Delta_g)$ Using $B_C(\tau_c)$

So far, we have seen that the Doppler parameter cutoff traces the gas temperature over a reasonable range of optical depth. We have shown this to be a consequence of the presence of some absorption lines that are primarily thermally broadened, and of the small dispersion of the gas

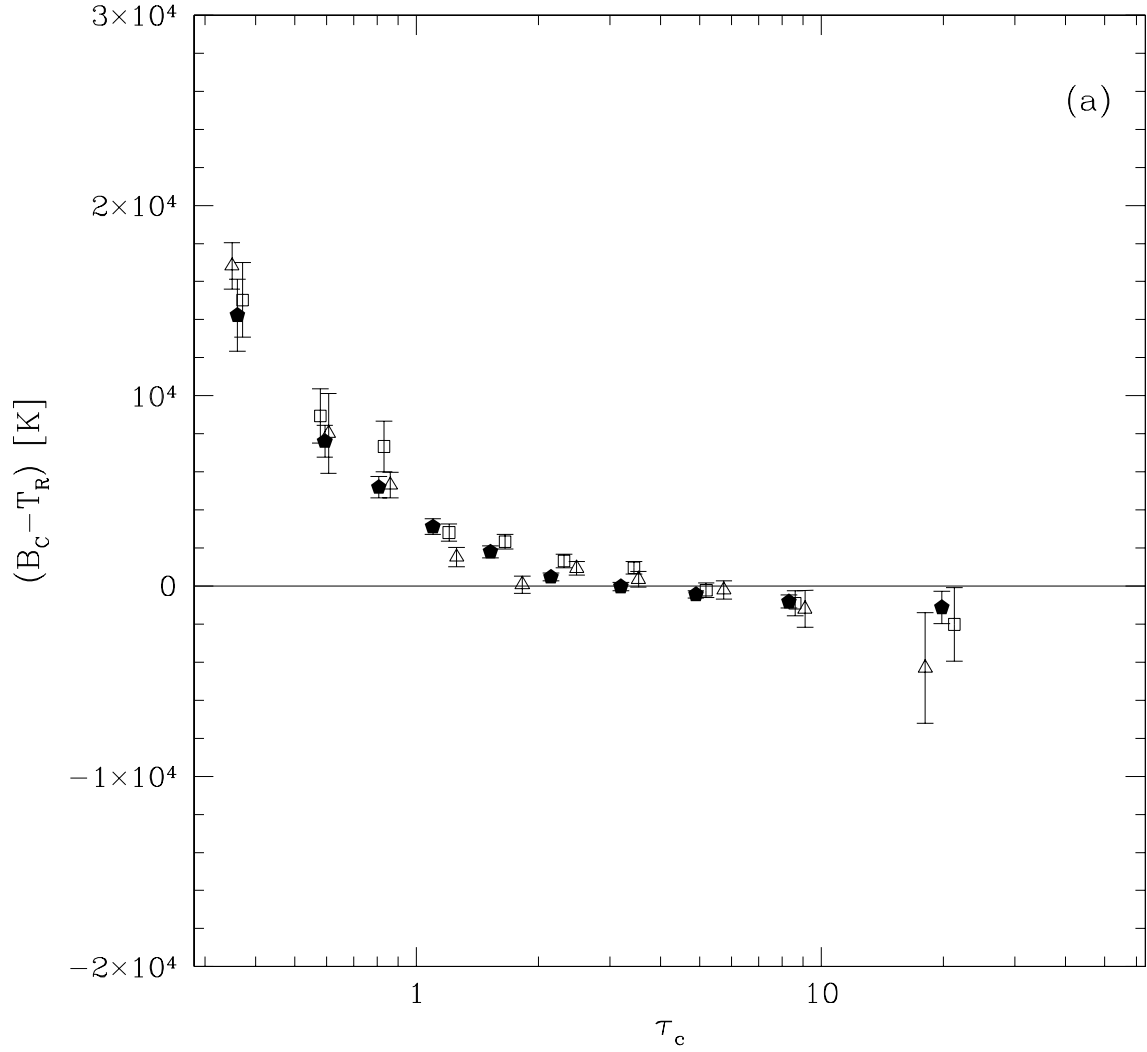
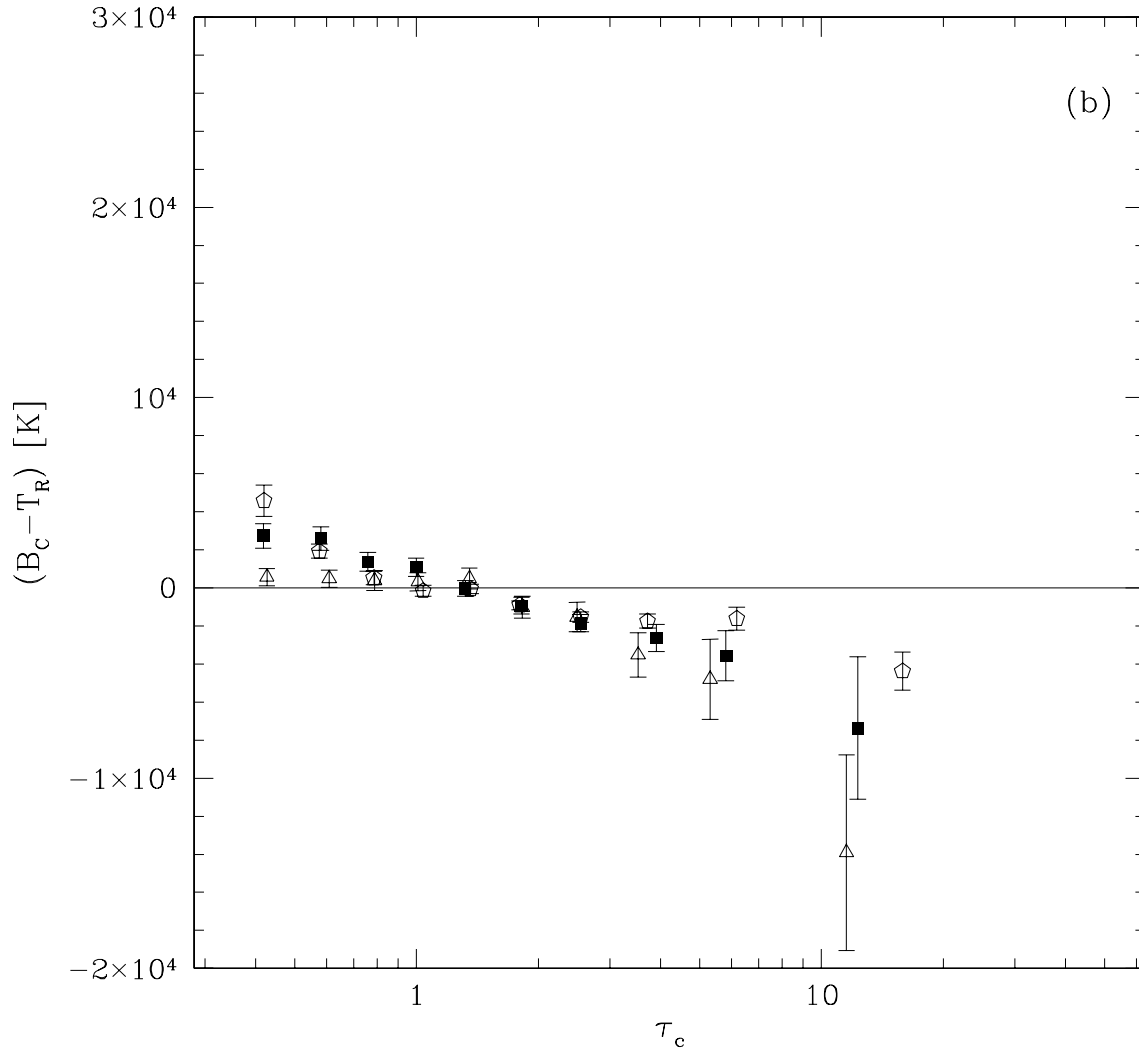
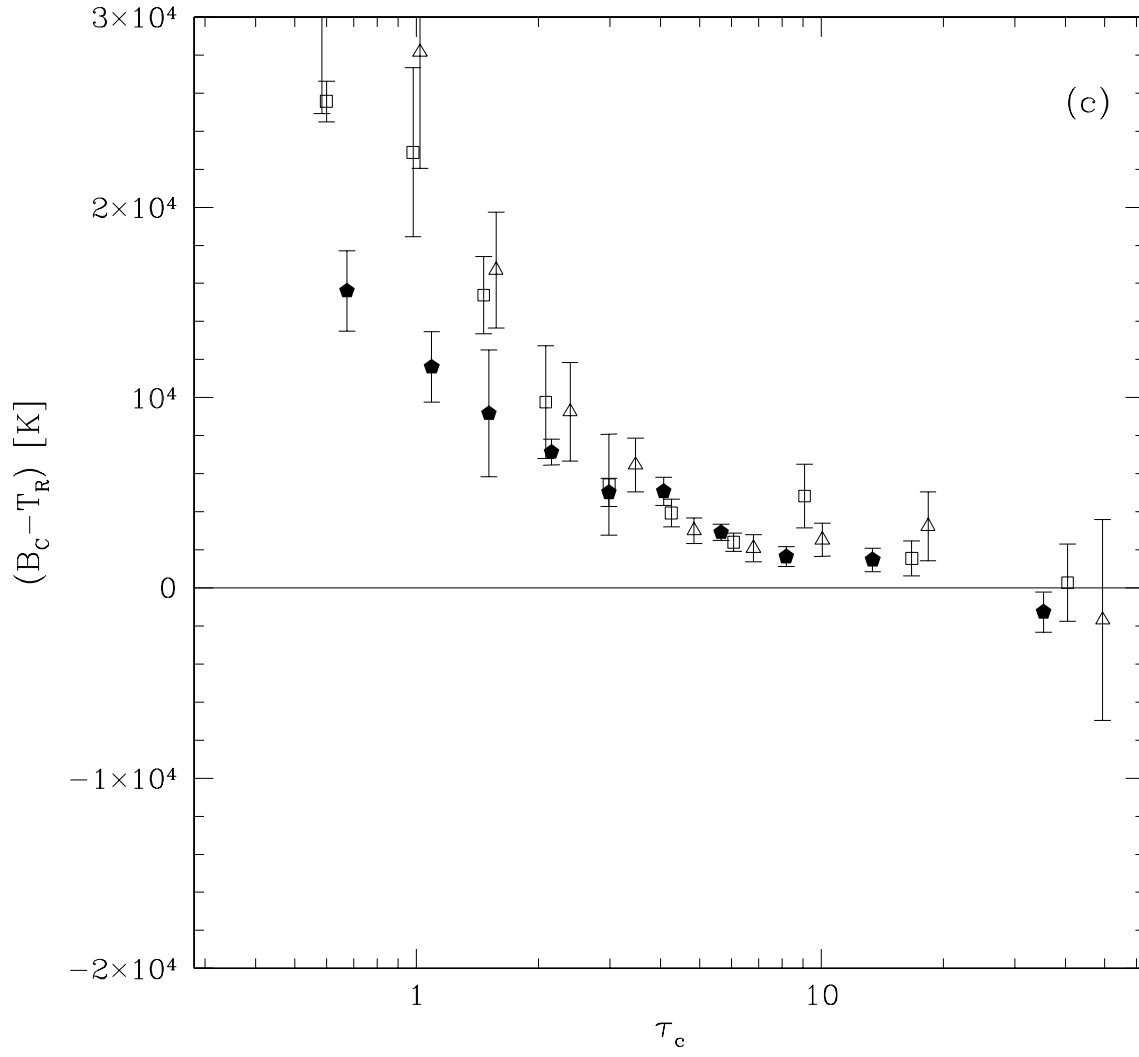


Fig. 9.— (*Pentagons, squares, triangles*): $B_C - T_R$, at the $z = (4, 3, 2)$ simulation output. The mean flux decrement, pixel size, and noise level is set to match the $\bar{z} = (3.0, 2.4, 3.9)$ observations in panels (a, b, c).





temperature. We therefore expect that this relation between B_C and T_R will not be significantly changed depending on the model adopted in the simulation, or when the numerical resolution is increased.

However, even over a restricted range of optical depth where B_C and T_R are best matched, the simulation predicts a difference between them, which we want to correct for when analyzing the observational data (although this correction could be model dependent, and will need to be compared with other simulations in future work). In addition, we need to relate the central optical depth τ_c to the optical-depth-weighted gas density of the absorber, Δ_b , in order to derive the $T - \Delta_g$ relation of the gas from the observed B_C as a function of τ_c . Given the limited amount of data that we will analyze in this paper, it will be sufficient to parameterize the $T - \Delta_g$ relation by a power-law,

$$T = T_\star (\Delta_g / \Delta_\star)^{\gamma-1} . \quad (6)$$

where Δ_\star is chosen to make the error on T_\star and $\gamma - 1$ uncorrelated. As discussed in §2.2.2, this power-law should be understood only as a fit to the true relation, which should be more complex. The power-law form will be adequate here given our error bars, but larger sets of data might be used to detect deviations from a power-law.

In this subsection we develop the method to derive the parameters T_\star and γ , given the determination of B_C at different optical depths.

5.4.1. Accounting for the Systematic Offsets $B_C - T_R$

To obtain an accurate estimate of the gas temperature from observations, the systematic differences between B_C and T_R shown in Figure 9 can be used to correct the observed B_C . However, this correction may be dependent on the model, and this dependence will not be known until a wide variety of additional simulations are analyzed. We therefore use only absorption lines over the range of τ_c where the offset between B_C and T_R is small ($|B_C - T_R| < 5000\text{K}$ for all three simulation outputs). The following optical depth ranges will be used: $0.41 < \tau_c < 5.4$ for $\bar{z} = 2.4$, $1.0 < \tau_c < 19$ for $\bar{z} = 3.0$, and $3.8 < \tau_c < 47$ for $\bar{z} = 3.9$.

For each fitted line obtained from the observations (within the accepted optical depth range), we determine a temperature correction at the optical depth of the line by linearly interpolating from the two adjacent points in Figure 9. The set of points used depends on the redshift bin of the observations and the simulation output we choose for the analysis. The corrected line width is $B' = B - \Delta T(\tau_c)$, where B is the observed line width, $\Delta T(\tau_c) = B_{C,S}(\tau_c) - T_{R,S}(\tau_c)$, $B_{C,S}(\tau_c)$ is the cutoff of the B distribution in the simulation, and $T_{R,S}(\tau_c)$ is the median temperature in the simulation at random points with gas density equal to the median density of the absorption lines satisfying $|B - B_C(\tau_c)| < 5000\text{K}$.

5.4.2. Translating τ_c into Δ_g

After the corrections just described, we have an estimate of the temperature as a function of τ_c . What we need, however, is the temperature as a function of Δ_g . This will be derived by using a transformation from τ_c to Δ_g that we obtain from the simulation. This introduces an inevitable model dependence in our measurement: the relation between τ_c and Δ_g , given a fixed flux decrement, should essentially be subject to the same uncertainties that appear in deriving the parameter $\mu \sim (\Omega_b h^2)^2 / \Gamma / H(z)$ (where Γ is the photoionization rate due to the cosmic background) from the observed mean flux decrement (see Rauch et al. 1997, Paper I).

Figure 10 is a scatter plot of the density and optical depth of the lines fitted from the $z = 3$ simulation output (with mean flux decrement matching the $z = 3$ observations). The crosses show Δ_g vs. τ_c for all of the lines, while the filled squares show only lines satisfying $|B - B_C(\tau_c)| < 5000\text{K}$, where $B_C(\tau_c)$ was determined for 10 optical depth bins as described earlier. The lines that determine the B cutoff (shown as squares) tend to have a higher optical depth than other lines at the same density, because of their lower velocity dispersion.

To obtain the $\Delta_g - \tau_c$ relation, we assign the median density of the lines in each optical depth bin that we use to measure the temperature (i.e., those with $|B - B_C(\tau_c)| < 5000\text{K}$) with the median τ_c of the same lines. We use interpolation to calculate the density corresponding to any value of τ_c for the fitted lines in the observed spectra.

One of the quantities affecting the $\tau_c - \Delta_b$ relationship is the density-temperature relation itself, essentially because the temperature affects the recombination coefficient, which then changes the neutral fraction at a given density. In order for our determination of the $T - \Delta_g$ relation to be self-consistent, we need to change the temperatures in the simulation so that they agree with the same $T - \Delta_g$ relation. We do this in the following way: after determining a preliminary $T - \Delta_g$ relation using the simulation with the true temperatures, we modify the temperature in every cell of the simulation using the formula

$$T'_i = T_i - T_\star (\Delta_i / \Delta_\star)^{\gamma-1} + T'_\star (\Delta_i / \Delta_\star)^{(\gamma-1)'} , \quad (7)$$

where T_i is the original temperature at cell i , T'_i is the modified temperature, T_\star and $\gamma - 1$ are the parameters of the original $T - \Delta_g$ relation of the simulation, and T'_\star and $(\gamma - 1)'$ are the parameters of the new $T - \Delta_g$ relation that we wish to impose. We then iterate the application of this formula until the modified $T - \Delta_g$ relation of the simulation matches the one from the observations. This modification of the temperatures in the simulation causes only a small change in the derived $T - \Delta_g$ relation (the value of T_0 is modified by only $\sim 5\%$).

5.4.3. Fitting for $\gamma - 1$ Without Binning

We now describe the method we use to fit the parameters T_\star and $\gamma - 1$ to the values of Δ_g and B' of a set of fitted lines. The simplest method would be to separate the lines in density bins,

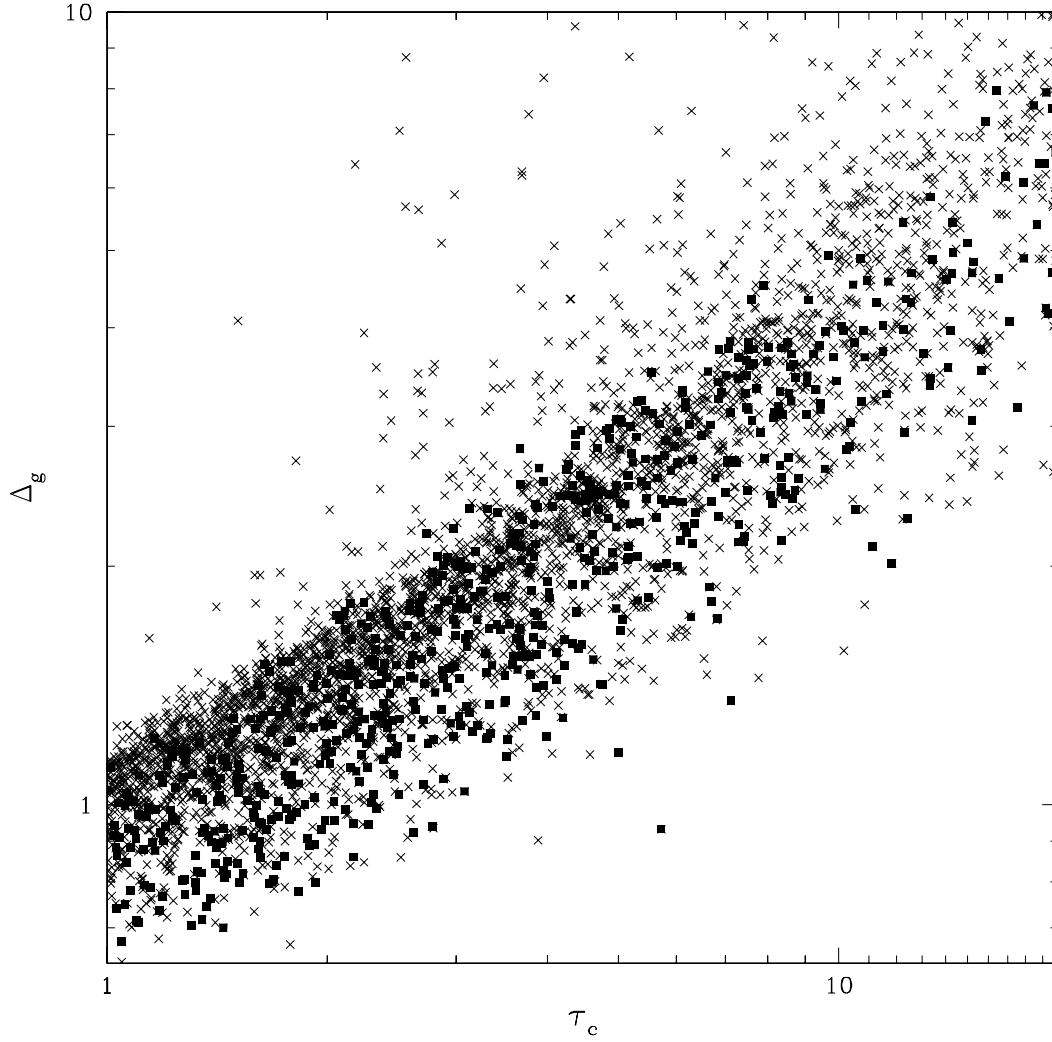


Fig. 10.— Δ_g vs. τ_c for a set of fitted absorption lines from the $z = 3$ simulation output. Crosses mark all the lines, squares indicate the lines with $|B - B_C(\tau_c)| < 5000\text{K}$.

measure the cutoff B_C in every bin, and then fit the power-law relation to the values of B_C obtained at every bin. However, the binning could result in a degradation of the measurement errors: at least 50 lines are needed to obtain a reasonable estimate of the cutoff B_C , and since our data yield only a few hundred lines for each redshift bin, the binning in line density would need to be very coarse.

There is a simple solution to this binning problem if the cutoff on the distribution of fitted lines, in the $B' - \Delta_g$ plane, is described by a power-law (recall that B' is the width of each fitted profile minus the expected non-thermal broadening at its optical depth, as described in §5.4.1). After we have associated a gas density Δ_g with each fitted line and corrected their temperatures using the simulation predictions, we rotate the absorption lines in the $B' - \Delta_g$ plane for many different assumed values of $\gamma - 1$, using the formula

$$B'' = B' - T_\star(\Delta_g/\Delta_\star)^{\gamma-1} . \quad (8)$$

For each assumed $\gamma - 1$, we apply the cutoff determination technique to the B'' distribution (without density binning) to find a value for the temperature and a maximum value for dP/dB [see eq. (5)]. As $\gamma - 1$ is varied, the best fit value of $\gamma - 1$ is the one that results in the maximum value of dP/dB , i.e., the sharpest cutoff on the B'' distribution.

Note that the value of T_\star used in equation (8) affects the size of the temperature changes in the rotation. We therefore also iterate in the determination of T_\star and γ by this procedure. In practice, the measurement of T_\star is barely affected by the rotation in equation (8), so a single iteration is sufficient.

Before presenting the results of applying our method to the observations, it will be useful at this point to summarize the full procedure we have described for measuring T_\star and $\gamma - 1$ from the B distribution of the fitted absorption lines at every redshift bin. This consists of the following steps:

1. Eliminate the absorption lines with τ_c outside the range where the temperature measurement is expected to be effective.
2. Correct the values of B for all of the remaining lines using the systematic offset predicted by the simulation (Figure 9).
3. Use the $\tau_c - \Delta_g$ relation in the simulation to associate a value of Δ_g with each fitted line.
4. Determine an initial estimate for T_\star and $\gamma - 1$ with the method of fitting the power-law cutoff in the B distribution as a function of τ_c that was just described.
5. Modify the $T - \Delta_g$ relation in the simulation to more closely approximate the relation measured from the observations.
6. Repeat steps 2-5 until the $T - \Delta_g$ relation measured from the observations matches the relation in the simulation.

6. ANALYSIS OF THE OBSERVED SPECTRA

We now apply our line-fitting method to the observed spectra. Table 3 lists, for each redshift bin, the redshift range (z_{min} to z_{max}) and mean redshift \bar{z} , the mean flux decrement \bar{F} , the mean noise, the total number of pixels, the total path length, the value of E_d we use to fit the lines, the total number of lines fitted, and the number of lines that we actually use to measure the gas temperature in the range of central optical depth from τ_{min} to τ_{max} .

The parameters (B, τ_c) of all the fitted lines are shown in Figure 11(a,b,c) for the redshift bins $\bar{z} = (3.9, 3.0, 2.4)$, as outlined crosses when the lines are not in any of the regions suspected to include metal lines, and as simple crosses when they are. For the quasar KP 77 (included in the redshift bin $\bar{z} = 2.4$), the analysis to identify potential metal lines was not done, so all lines from this quasar are shown as outlined crosses. The lower cutoff on the B distribution is clearly visible to the eye at all three redshifts, especially when the metal lines are ignored.

In Figure 12(a,b,c) we compare the B histograms of the observed lines, within the ranges of optical depth that we will use for the temperature measurements, to the B histograms of fitted lines from the simulation outputs with redshifts closest to the means of the observations, in the same optical depth ranges. The observed absorption lines obviously have higher temperatures than the simulated ones in all three cases.

It is interesting to compare directly $B_C(\tau_c)$ from the observations and from the simulation, before we determine $T = T_\star(\Delta_g/\Delta_\star)^{\gamma-1}$ using the more involved method described in §5.4. Figure 13(a,b,c) shows the values and errors of B_C measured from the observations and the simulation output that is nearest in redshift, using lines over the optical depth bins indicated by the horizontal error bars (the optical depth bins contain equal numbers of observed lines). The vertical dotted lines indicate the optical depth range that we use for the final temperature measurement (for the $\bar{z} = 3.9$ analysis, the upper limit on τ_c is outside of the figure, and eliminates a negligible number of lines). Recall (Figure 9) that we do not expect the points with lower τ_c to accurately reflect the real temperature, except at the lowest redshift. The observed lines again appear to be hotter than the simulated lines. These results are listed in Table 4, along with the temperature offset ΔT used as a correction to the temperature (see §5.4.1) and the estimated gas densities, Δ_g , that we find once the $T - \Delta_g$ relation in the simulation has been adjusted to match the observed one (determined below). If more observed spectra were available, this method of binning in optical depth would be preferable to the method in §5.4 because it does not require the assumption of a power-law $T - \Delta_g$ relation. Each bin in optical depth would be associated with the density listed in Table 4, and the value of B_C would be corrected by the listed ΔT .

We now determine T_\star and $\gamma - 1$ by the method described in §5.4. In order to obtain the $\tau - \Delta_g$ relation and the temperature offsets ΔT , we can use any of the three simulation outputs at $z = 2, 3, 4$ for any of the three redshift bins in which we have divided the data (although we change the mean flux decrement of the simulated spectra to the observed one at each redshift bin). The different redshift outputs of the simulation are approximately equivalent to assuming

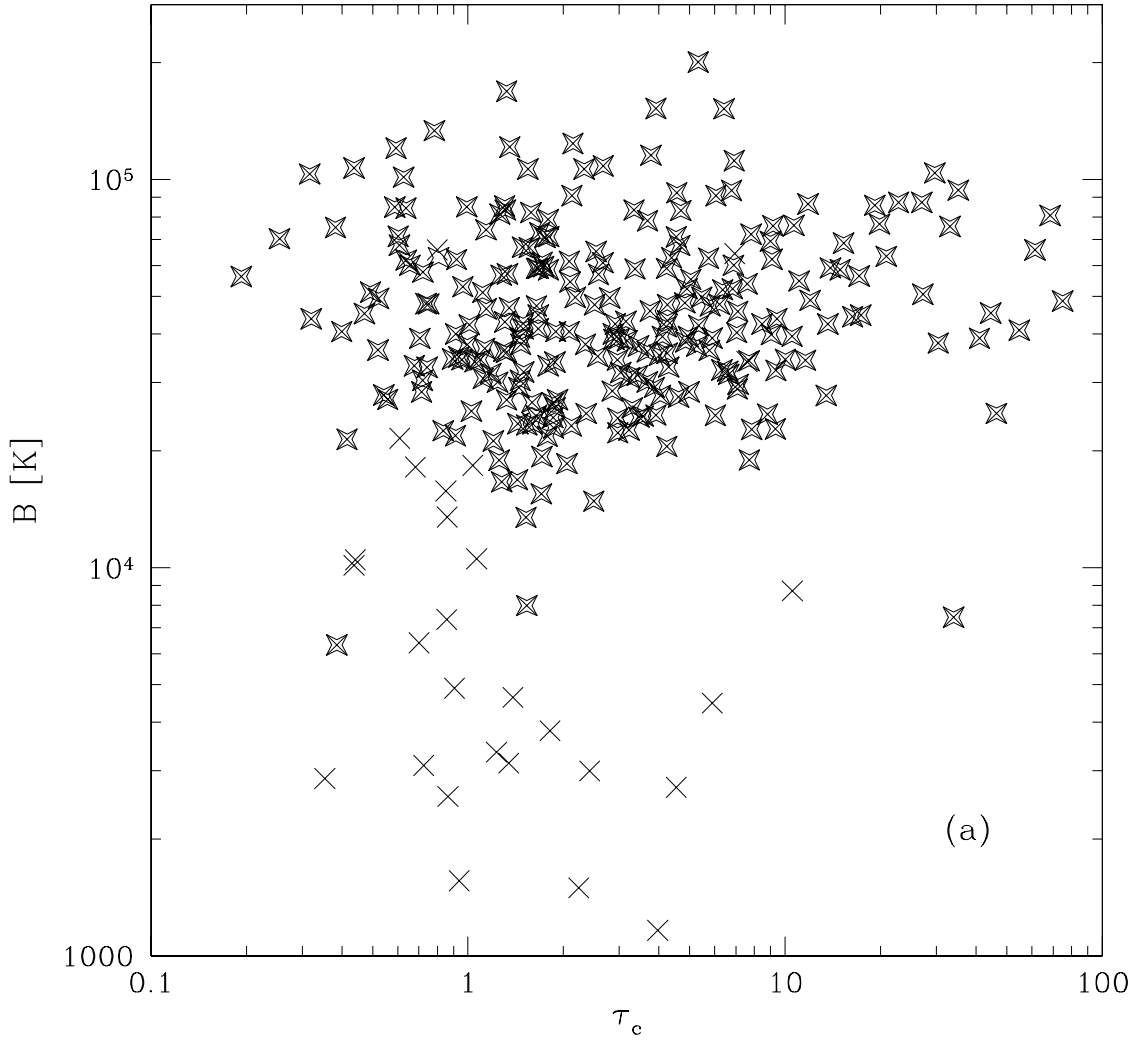
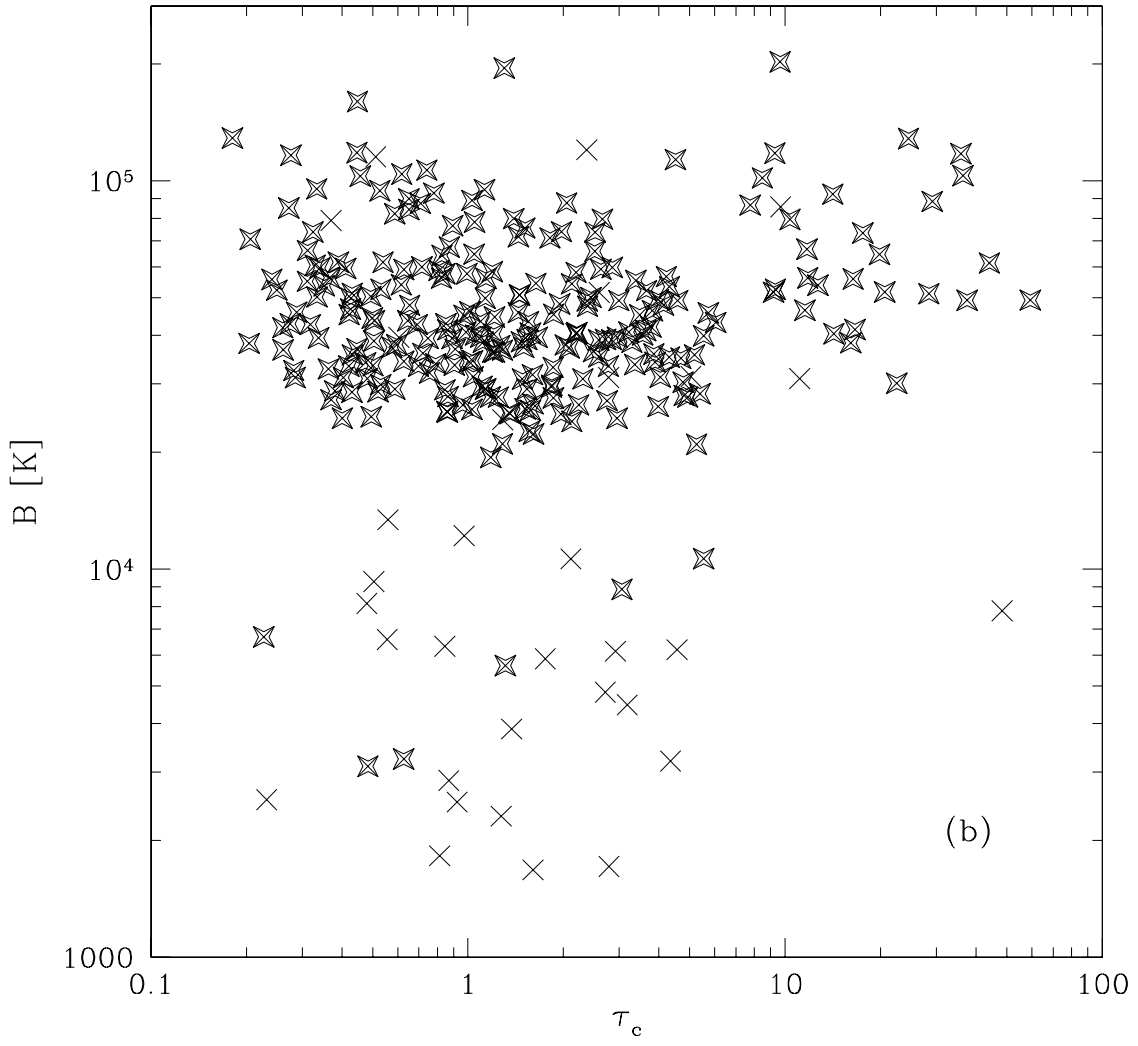
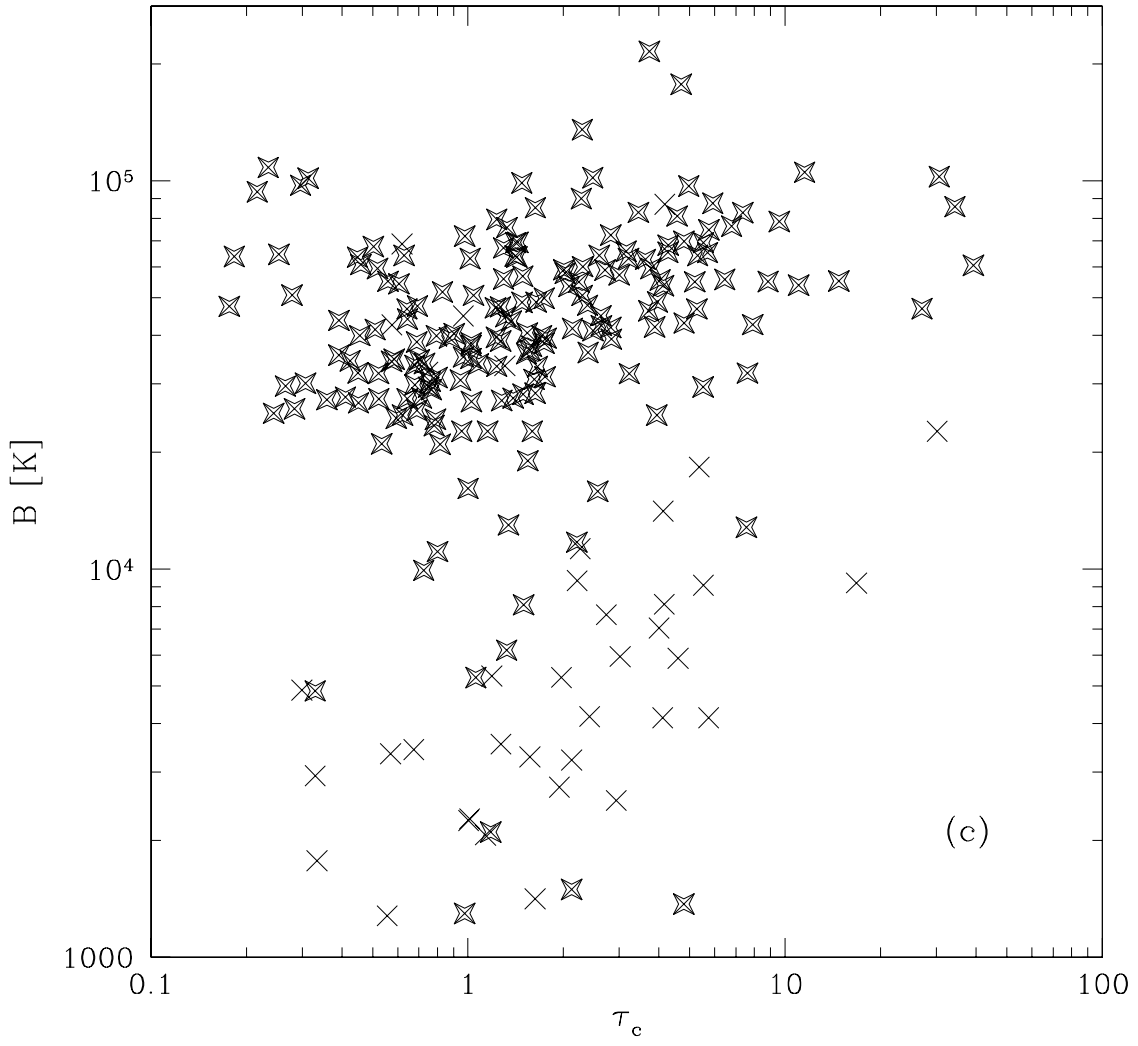


Fig. 11.— (a, b, c) Fitted lines in the observed spectra at $\bar{z}=(3.9, 3.0, 2.4)$. Outlined crosses are lines that are not in regions containing potential metal lines.





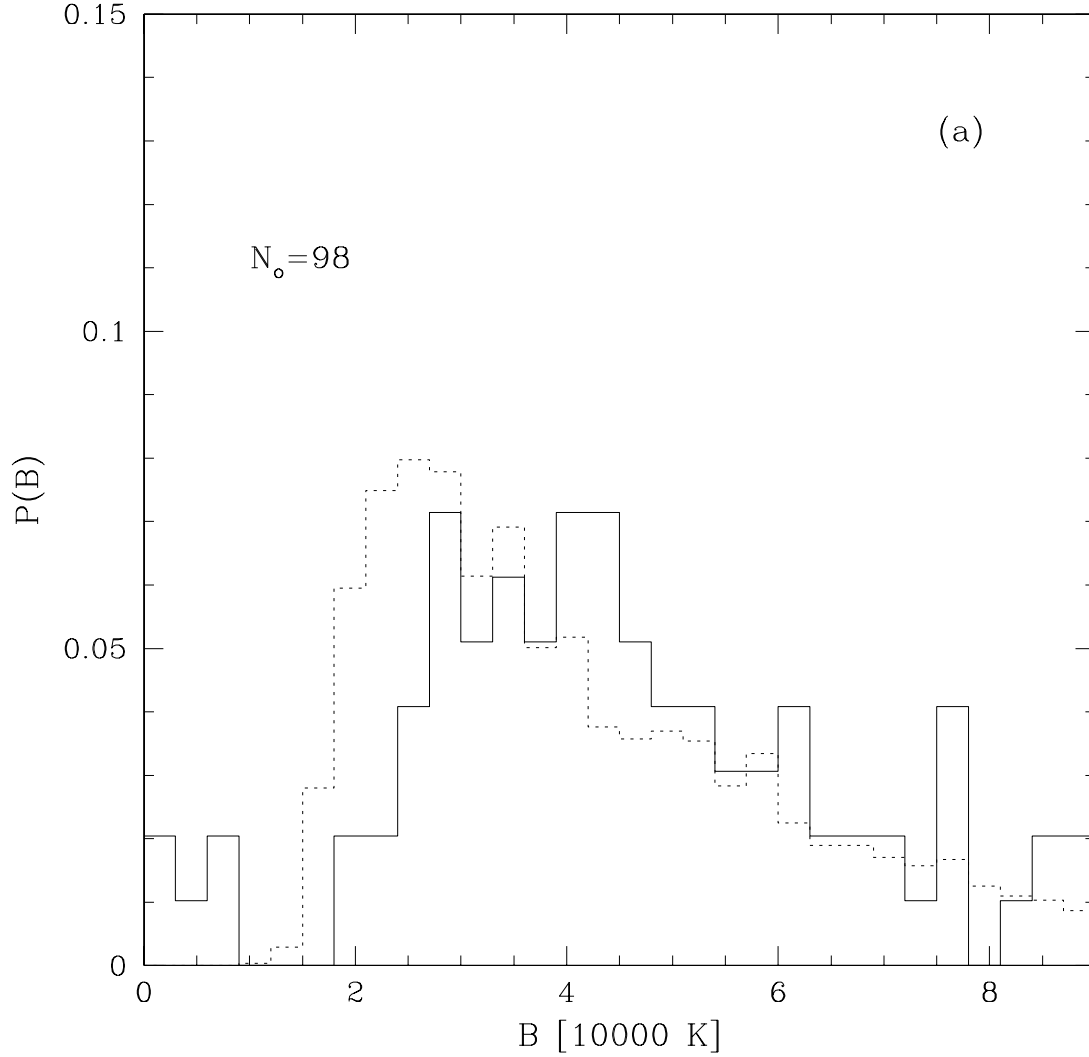
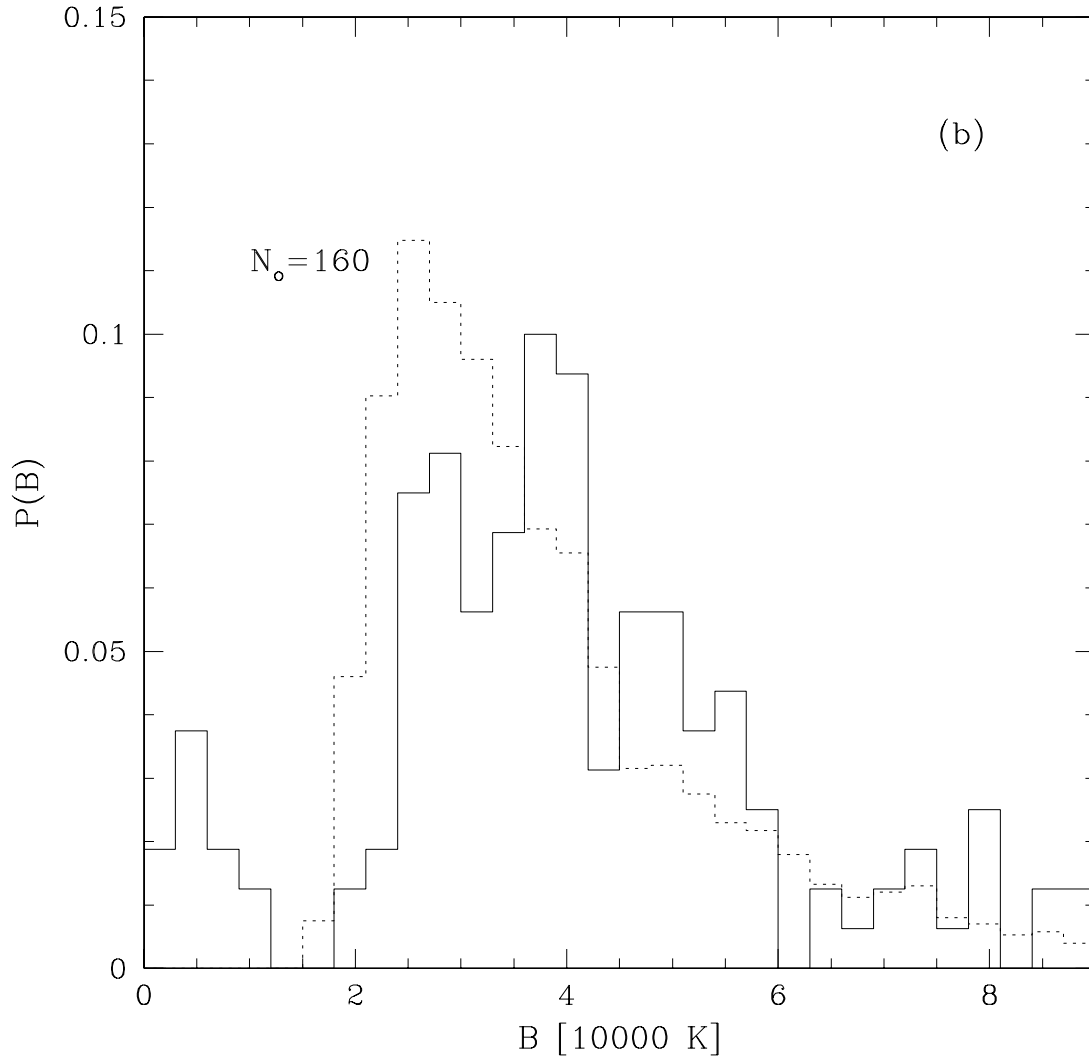
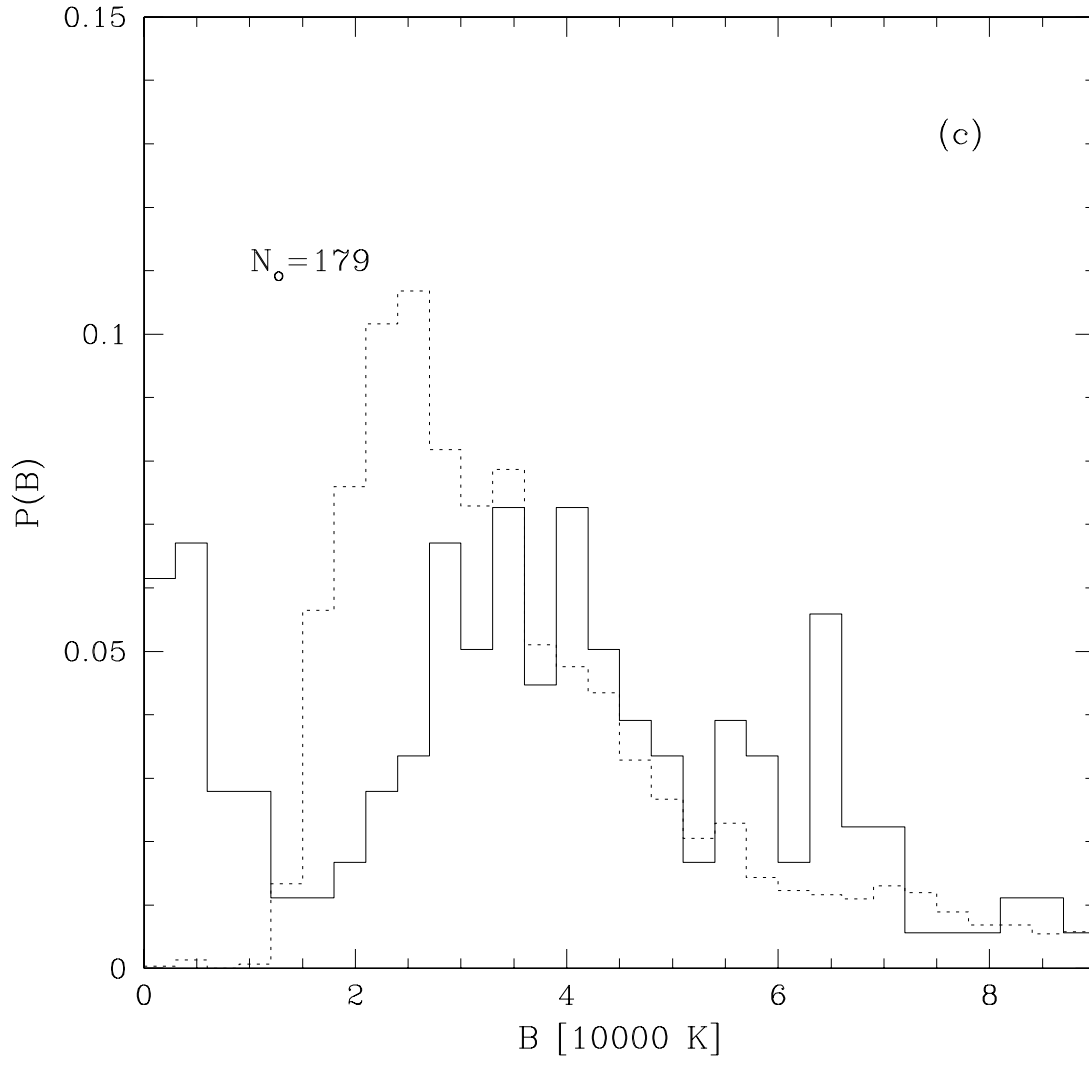


Fig. 12.— Distribution of B of fitted absorption lines. (a) *Solid line*: observed lines at $\bar{z} = 3.9$, with $3.8 < \tau_c < 47$. *Dotted line*: Lines from simulation output at $z = 4$, with $3.8 < \tau_c < 47$. (b) Same as (a) for the $\bar{z} = 3$ redshift bin and $z = 3$ simulation output, with $1.0 < \tau_c < 19$. (c) Same as (a) for the $\bar{z} = 2.4$ redshift bin and $z = 2$ simulation output, with $0.41 < \tau_c < 5.4$. N_o is the total number of observed lines in each histogram.





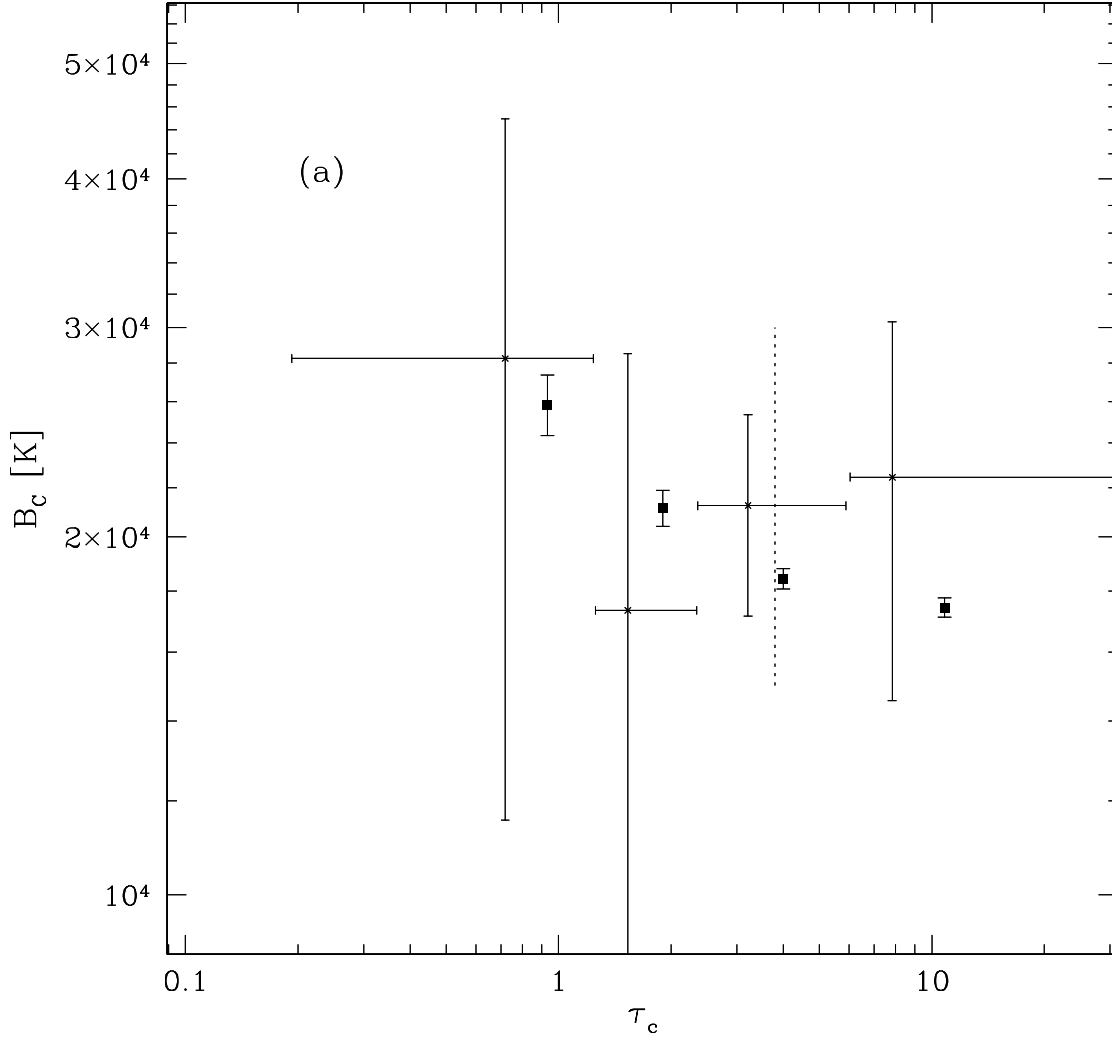
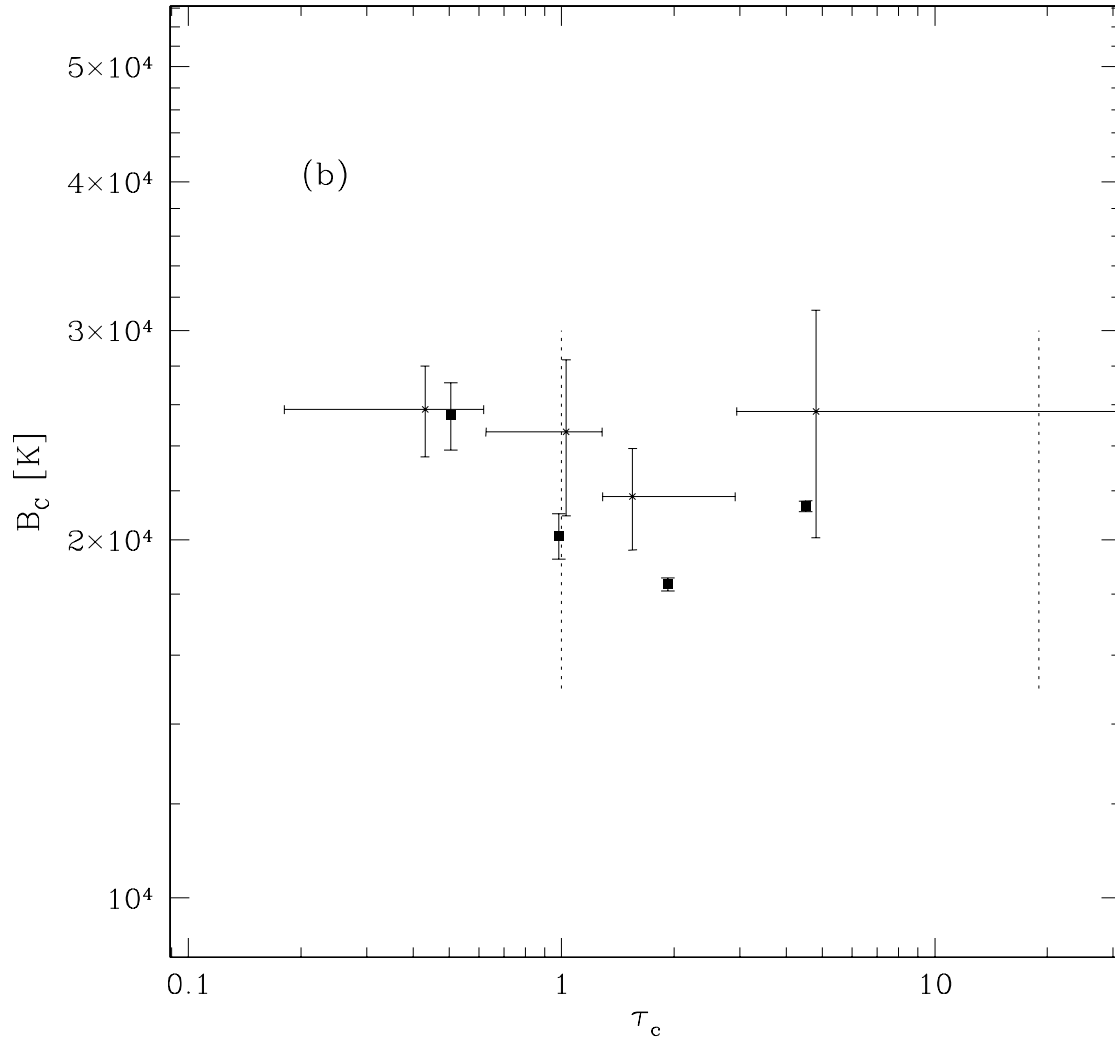
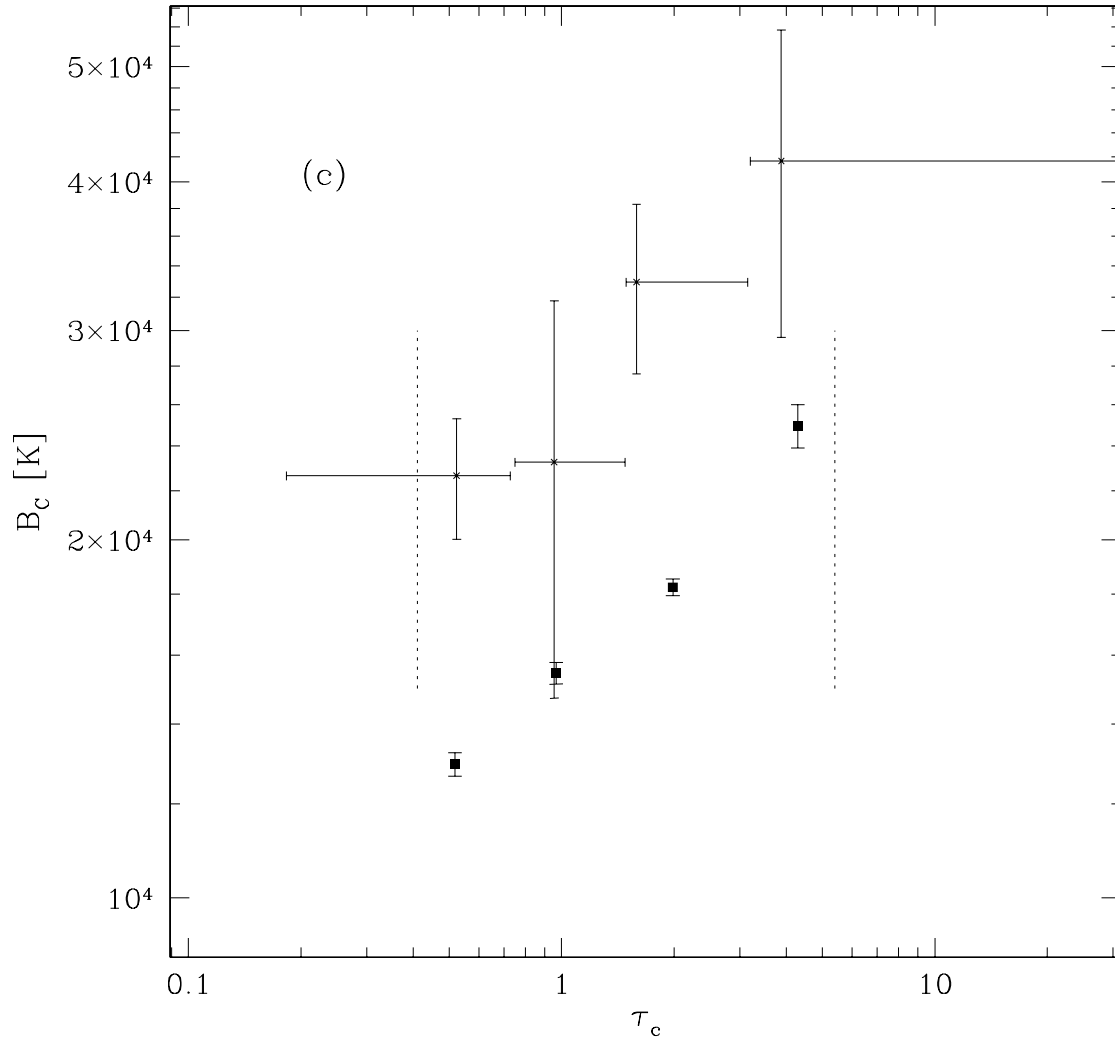


Fig. 13.— (a, b, c) *Crosses with large error bars*: $B_C(\tau_c)$ for observed lines at $\bar{z}=(3.9, 3.0, 2.4)$. *Squares with small error bars*: $B_C(\tau_c)$ from the simulation at $z=(4, 3, 2)$. Only lines in the range of τ_c between the vertical dotted lines [or to the right of the single dotted line in (a)] are used for our final temperature measurement.





different models with a different amplitude of the power spectrum (Paper I), so we can use the different outputs to check that our measurement of the temperature is not greatly sensitive to the model that is assumed. Paper I found that the amplitude of the initial density perturbations in our simulation needs to be reduced by about 15% to agree with the observed power spectrum of the transmitted flux, meaning that the simulation output at $z = 4$ has fluctuations that most closely match the observed ones at $\bar{z} = 3$, and are slightly higher than the observed fluctuations at $\bar{z} = 3.9$. The $\bar{z} = 2.4$ observational bin is closest in amplitude to the simulation output at $z = 3$. The most reliable temperature results should therefore be obtained by using the $z = (4, 4, 3)$ simulation outputs to analyze the $\bar{z} = (3.9, 3.0, 2.4)$ observations, but we shall also give results for $\bar{z} = (3.0, 2.4)$ analyzed using the $z = (3, 2)$ simulation outputs.

The result at $\bar{z} = 3$, using the $z = 4$ simulation output to predict the $\tau - \Delta_g$ relation and the necessary correction for non-thermal broadening, is:

$$T = [20200 \pm 1300] \left(\frac{\Delta_g}{1.37 \pm 0.11} \right)^{[0.29 \pm 0.30]} \text{ K}, \quad (9)$$

where the error bars on T_\star and $\gamma - 1$ are uncorrelated (which defines Δ_\star). The error bar on Δ_\star reflects only the uncertainty in the Paper I determination of the mean flux decrement, which affects the relation between density and optical depth. This result implies $T_0 = 18400 \pm 2100\text{K}$, where T_0 is the temperature at the mean density. The pivot density, $\Delta_\star = 1.37$, corresponds to an optical depth $\tau_\star = 1.83$ (from the relation obtained as described in §5.4.2) When we repeat the fitting using the $z = 3$ simulation output we find $T = [19600 \pm 1500](\Delta_g/[1.24 \pm 0.10])^{[0.33 \pm 0.28]}\text{K}$, or $T_0 = 18300 \pm 1800\text{K}$ ($\tau_\star = 1.74$). The difference between the two values for Δ_\star , 1.37 using the $z = 4$ simulation, and 1.24 using the $z = 3$ simulation, are mostly a reflection of the different optical depth normalizing factors (i.e., rescalings of the baryon density or the strength of the ionizing background) needed to match the observed mean flux decrement. The normalizing factor is smaller for the $z = 4$ simulation, giving a larger Δ_\star for the same optical depth, because the density fluctuations are of lower amplitude, leading to less saturated absorption and more absorption in voids (see Paper I for a more detailed discussion of the optical depth normalizing factor).

All the results obtained at the three redshift bins are listed in Table 5. The data analysis at $\bar{z} = 2.4$ and $\bar{z} = 3.9$ is similar to the analysis at $\bar{z} = 3$, except for the differences that we mention below.

The temperature results at $\bar{z} = 2.4$ differ by ~ 2000 K when the $z = 2$ simulation output is used instead of the $z = 3$ output, once the measured values of T_\star for the two are extrapolated to the same density. Most of this difference results from the difference in Δ_\star , and the relatively high value of $\gamma - 1$ that is obtained at $\bar{z} = 2.4$. The difference in Δ_\star is caused by the different amplitudes of density fluctuations in the two simulation outputs, so we expect that the temperature derived using the $z = 3$ simulation output, which has the correct amplitude of fluctuations, is more reliable (see Paper I).

In order to see the evolution of the temperature with redshift, we need to obtain the temper-

ature at a fixed over-density at each redshift. It is useful to obtain the temperature at the mean density, T_0 , to compare our results to other work. However, the values of Δ_* are close to $\Delta_g = 1.4$ at all three redshift bins, and we can therefore have a more robust result for the temperature evolution if we examine the temperature at $\Delta_g = 1.4$, which we denote as $T_{1.4}$ in Table 5.

We note here that, because of the small range of optical depth used at $\bar{z} = 3.9$, at this redshift we were forced to smooth the B'' histograms with a Gaussian filter of width $\sigma_B = 7000\text{K}$, instead of our standard $\sigma_B = 5000\text{K}$, in order to avoid problems with multiple, approximately equivalent, maxima of equation (5) as $\gamma - 1$ is varied.

The primary results of this paper, the measurements of $T_{1.4}$ and $\gamma - 1$, are summarized in Figures 14 and 15, respectively. These show two important conclusions: first, the temperatures are higher than the value expected if photoionization heating in equilibrium is the only heating source. Second, we find no evidence for a rapid change of the temperature with redshift.

7. DISCUSSION

This paper presents a measurement of the temperature-density relation of the intergalactic gas in the redshift range $2.4 < z < 4$. The new method we have developed to perform this measurement is based on the same general idea as the previous work by Schaye et al. (1999), Ricotti et al. (2000), and Bryan & Machacek (2000): provided that there is a tight relation between the temperature and density of the gas, absorption lines of similar central optical depth should have little dispersion in their thermal broadening, and the varying line widths should correspond to variable amounts of hydrodynamic broadening. Occasionally, some absorption lines will be subject to only a small degree of hydrodynamic broadening; this will typically happen when most of the atomic hydrogen occurs near a velocity caustic along the line of sight. We therefore expect the histogram of line widths to show a rapid increase near the value of the Doppler parameter corresponding to the gas temperature. In the absence of noise, every line should be wider than the thermal broadening width, so at least an upper limit to the temperature can be obtained unambiguously.

The tests we have performed using a numerical simulation of the Ly α forest, based on a CDM model that successfully reproduces the observations of large-scale structure at present, confirm this general idea. However, they show that this method to recover the gas temperature works efficiently only over a limited range of line optical depths, which corresponds approximately to a range of gas over-density $1 \lesssim \Delta_g \lesssim 3$. At lower densities, the gas is generally in Hubble expansion and this effect dominates the contribution to the line widths in essentially all the lines. The minimum line widths can therefore only provide an upper limit to the temperature of this low-density gas. Of course, the simulation can in principle be used to correct for the effect of line broadening due to Hubble expansion, and to obtain the temperature by subtracting the hydrodynamic contribution to the minimum line widths. However, the results can then strongly depend on the assumed model and the numerical resolution of the simulation, especially as the thermal broadening becomes a

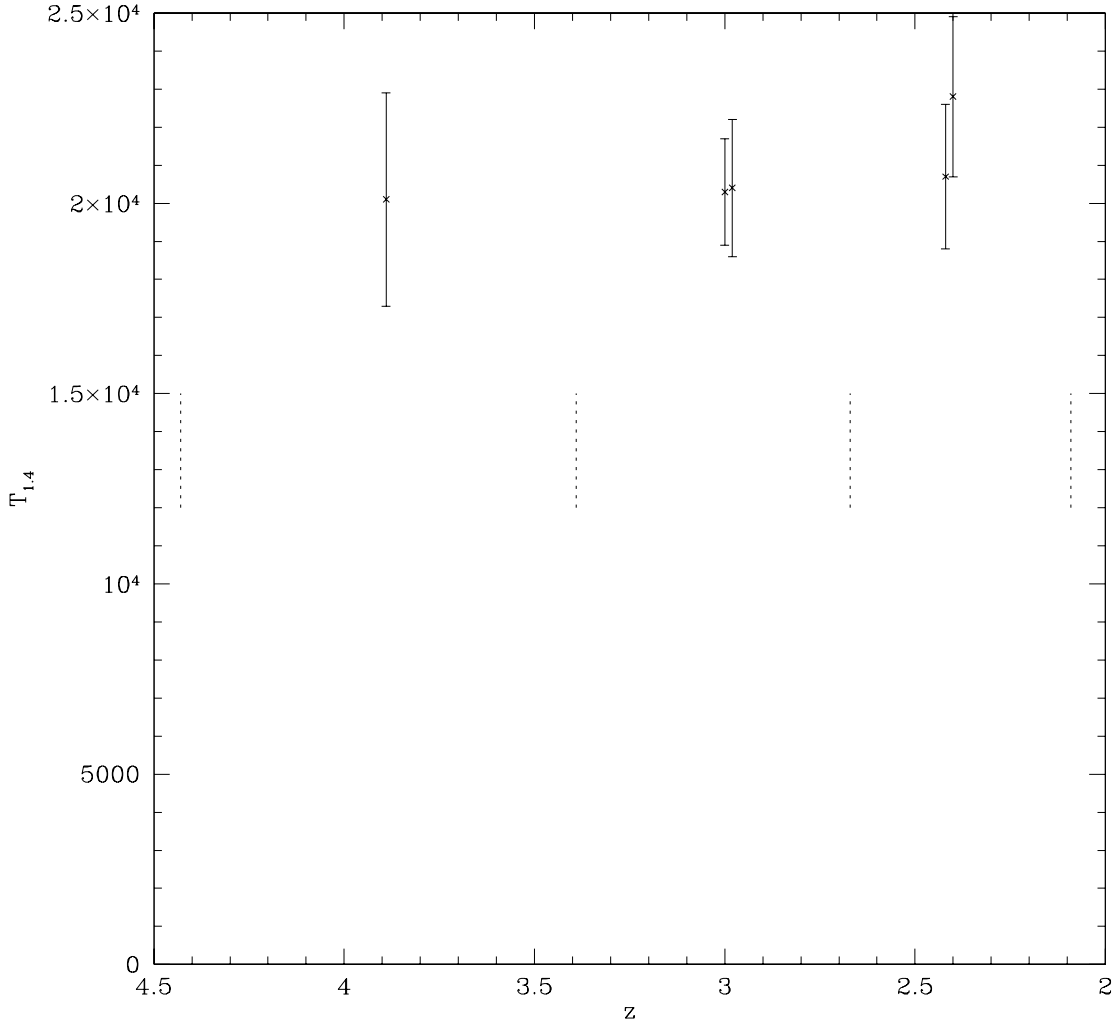


Fig. 14.— The observed temperature at $\Delta_g = 1.4$. The two points at $\bar{z} = 2.4$ and $\bar{z} = 3.0$ (offset slightly to distinguish them) show the result of using two different simulation outputs to analyze each of these redshift bins. The left and right points at $\bar{z} = 2.4$ are for the $z = 3$ and $z = 2$ outputs, respectively. The left and right points at $\bar{z} = 3.0$ are for the $z = 4$ and $z = 3$ simulation outputs. The vertical dotted lines show the boundaries of the redshift bins.

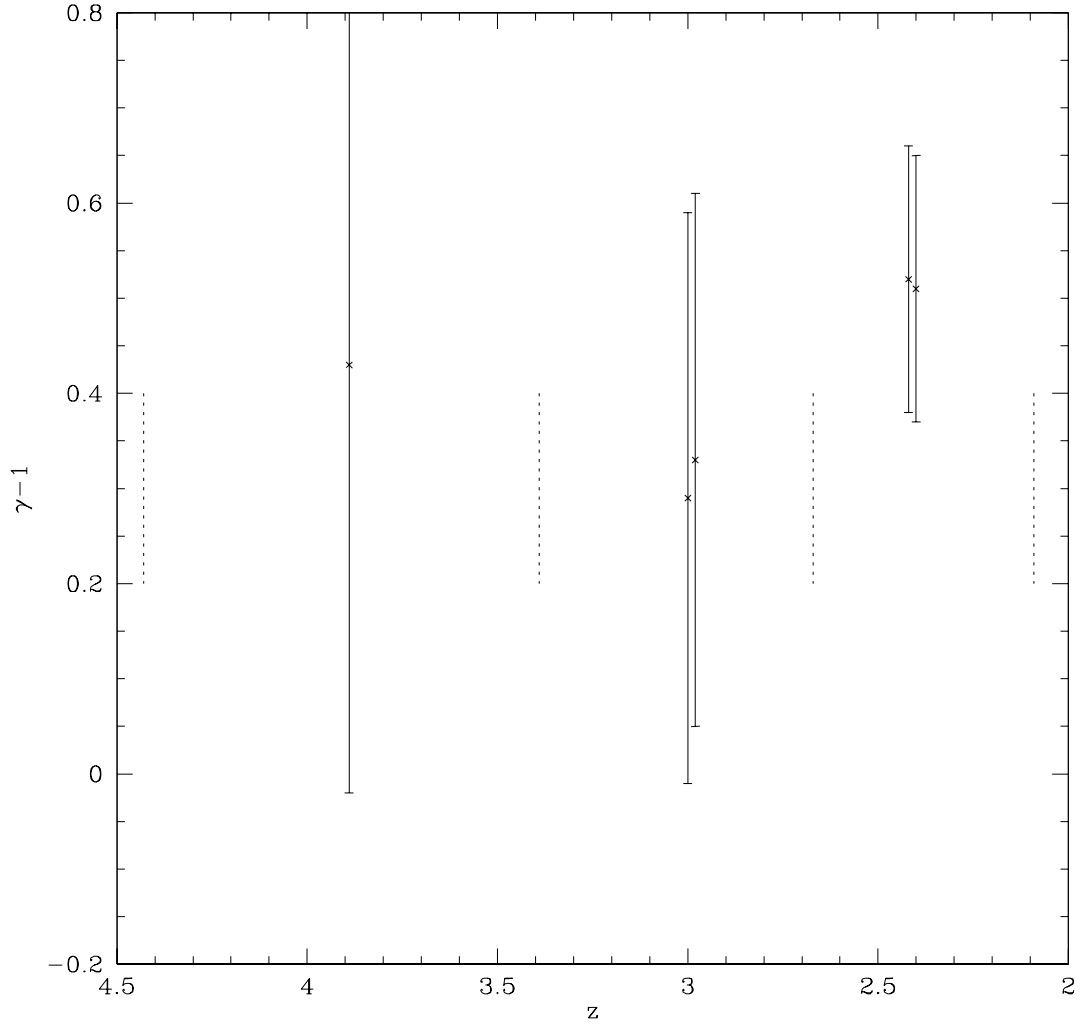


Fig. 15.— Similar to Figure 14 except here we plot the results for $\gamma - 1$.

small effect compared to the expansion.

At very high densities, the increasing dispersion of the temperature at a given gas density can result in a large difference between the typical gas temperature and the “lower cutoff” in the line width histogram. This implies again that the recovery of the median gas temperature from the distribution of line widths is highly sensitive to the model assumptions that affect the temperature dispersion and the turbulent motions in the gas.

There are two main differences between the method we use to measure the gas temperature, and that used by previous authors. First, our line detection algorithm avoids the necessity of the Voigt-profile fitting method to “deblend” lines, by simply throwing out any “absorption lines” that do not correspond to a clearly identified minimum in the transmitted flux, or that do not have a large enough region around that minimum that is adequately fitted by a simple Gaussian in optical depth. In the method we use here, every line width is essentially a measurement of the second derivative around a minimum in the flux. This is one important reason why the total number of lines we identify is much lower than Schaye et al. (2000), even though we use nearly the same data set. The second difference is that we restrict the absorption lines we use to lie within the range of central optical depth where the correction that needs to be applied to the temperature measured from the histogram of line widths (as described in §5.4.1) is small.

These differences explain our substantially increased error bars in measuring T_0 and γ , relative to those of Schaye et al. (2000). However, we believe our error bars are more reliable and model-independent, for the reasons we have discussed. We also note here that, even though we cannot rule out a substantial change of the temperature we have measured depending on the numerical simulation of the Ly α forest that is used for comparing to the observational data, this possibility appears unlikely for several reasons, in addition to the arguments explained before about the small size of the correction ΔT that needs to be applied to the line width cutoff B_c to obtain the gas temperature (see §5.4.1). The gas temperature of the simulation we use is lower than that observed only by a small amount: in the simulation, the temperature at the mean density is $T_0=(14000, 15800, 12800)$ K at $z=(4, 3, 2)$, while our measurement from the observational data is $T_0 = (17400 \pm 3900, 18400 \pm 2100, 17400 \pm 1900)$ K for $\bar{z}=(3.9, 3.0, 2.4)$. The amplitude of the flux power spectrum of the simulation is also very close to the observationally determined one (Paper I). We have also shown that we obtain nearly identical results for the temperature measurement when using different simulation outputs to analyze the same observations (see Figures 14 and 15) meaning that the dependence on the amplitude of the power spectrum is weak. Our result for the gas temperature might also be affected by the limited resolution of the simulation we use (with a comoving cell size of 35 Kpc). We have not yet performed a convergence test for the effects of resolution on the Ly α forest; however, Schaye et al. (2000) find that a mean particle spacing of ~ 45 Kpc in their SPH simulations is sufficient for convergence.

We now compare our results for the evolution of the gas temperature with previous measurements. Ricotti et al. (2000) find a temperature at the mean density (from their Figure 12b)

$T_0 \simeq (18600_{-6900}^{+10900}, 23400_{-5200}^{+10400}, 17000_{-9600}^{+22800})\text{K}$, at $z \simeq (3.6, 2.75, 1.9)$. Considering their large statistical error bars, our results appear to agree well with theirs, although the true temperature at $z \simeq 2.75$ must be at the low end of their error bar. Schaye et al. (2000) give their temperature results as 16 separate points, in their Figure 5. We read off their points in each of our redshift bins and create error weighted averages for comparison with our results, finding $T_0 \sim (12200 \pm 1700, 17300 \pm 1400, 14000 \pm 1300)$ at $z \sim (3.75, 3.2, 2.4)$. In order to compare these with our temperatures, which have lower errors at $\Delta_g = 1.4$, we extrapolate the Schaye et al. (2000) results to $\Delta_g = 1.4$ using their measured value of $\gamma - 1$, obtaining $T_{1.4} \sim 13600 \pm 2000\text{K}$ at $\bar{z} \sim 3.75$. Our result at $\bar{z} = 3.9$, $T_{1.4} = 20100 \pm 2800\text{K}$, is higher than theirs by $\sim 1.9\sigma$. Because of this, we do not find evidence for the increase of the temperature with time between $z = 4$ and $z = 3$ that Schaye et al. (2000) reported. Our results are consistent with a constant temperature.

Actually, the data set analyzed by Schaye et al. (2000) is almost identical to the one we analyze in this paper, with 7 of the 10 quasars used in the two papers being identical. However, our methods of analysis are very different, so that even the statistical error bars from the two analysis are largely independent. The main difference, as mentioned before, is in the number of lines that are identified. For example, we use 98 lines to measure the temperature in our $z > 3.4$ bin, while Schaye et al. (2000) use about 550 lines in a comparable bin, even though $\sim 80\%$ of the data that they use is identical to ours.

7.1. HeII Reionization as a Heating Mechanism

Is the value of the temperature we have measured in agreement with the known sources of heating and cooling in the intergalactic gas? The evolution of the temperature is determined by the equation:

$$\frac{d \log T}{H dt} = -2 \left(1 - \frac{1}{3} \frac{d \log \Delta}{H dt} \right) + \frac{2}{3kHT} (L_{He} + L_H - L_{CMB} - L_R - L_{ff} - L_a), \quad (10)$$

where the cooling and heating rates per particle are denoted as follows: L_{He} is the heating by He II photoionization, L_H is the heating by H I photoionization, L_{CMB} is the cooling off the microwave background, L_R is the cooling by recombination, L_{ff} is the cooling by free-free emission, and L_a is the cooling due to line excitation and collisional ionization. We have separated the terms for He II and H I photoionization because He II plays a dominant role for heating, but the other cooling terms include both hydrogen and helium.

To see what the important terms for the thermal balance of the IGM are, we now evaluate all the heating and cooling terms at the conditions where we have measured the temperature most accurately: a temperature $T = 20000\text{ K}$ at a gas density $\Delta = 1.4$, at $z = 3$. It is convenient to define the quantities $T' \equiv 2/(3kHT)L$, for each subscript corresponding to every heating and cooling term. We assume the model $\Omega_b h^2 = 0.019$, $\Omega_0 = 0.3$, $\Lambda_0 = 0.7$, and $H_0 = 65\text{ km s}^{-1}\text{ Mpc}^{-1}$. We evaluate first the total cooling: the dominant term is adiabatic cooling, which is equal to -2 on

the right-hand-side of equation (10) if we assume a rate of expansion equal to the Hubble rate (i.e., a constant Δ). This assumption is of course not exact; every gas element expands at a different rate, causing a dispersion in the temperature-density relation. However, at a density $\Delta = 1.4$, the average rate of expansion is in fact not very different from the Hubble rate. In addition, when we consider the evolution of the temperature at a fixed Δ , the $\partial T/\partial \Delta$ term in the total temperature derivative of the left-hand-side of equation (10) should partly compensate for the effect of expansion (canceling it exactly if $\gamma - 1 = 2/3$).

The next most important contribution is cooling off the microwave background, which is given by $T'_{CMB} = (8\sigma_T a T_{CMB}^4)/(3Hm_e c)(n_e/n) = 0.58$ (where σ_T is the Thompson cross section, m_e the electron mass, n_e the electron density, and n the total particle density). Notice that this term becomes more important at higher redshift, growing as $(1+z)^{5/2}$. We compute the other cooling rates using the formulae given in Black (1981). Recombination yields $T'_R = 0.22$, and free-free emission $T'_{ff} = 0.08$. The atomic processes of line cooling and collisional ionization are completely negligible at this low density, for the H I photoionization rate $\Gamma \sim 10^{-12} \text{ s}^{-1}$ that is obtained from the observed abundance of quasars. The total cooling rate is therefore $T' = 2.88$. If this temperature is being kept roughly constant, as indicated by the measurement we have presented here, then the heating terms should approximately balance the total cooling.

To evaluate the heating rate, we first assume ionization equilibrium; we will discuss later how the heating from He II can be increased if the He II reionization is still in progress. The heating term due to ionization can then be expressed in terms of the recombination rate: $L_H = \langle E_H \rangle (\alpha_H n_e)(n_H/n)$, and the analogous expression for He II, where α_H and n_H are the recombination coefficient and the number density of hydrogen, and E_H is the mean energy of the absorbed photons minus the ionization potential. The mean energy E_H depends on the spectrum of the ionizing background, and we evaluate it as follows: assuming a background intensity per unit frequency $J_\nu \propto \nu^{-\beta}$ from the ionization edge at ν_0 to some maximum frequency $\nu_m = q_m \nu_0$, and approximating also the photoionization cross section as $\sigma(\nu) \propto \nu^{-3}$, we find

$$\langle E_H \rangle = I_H \left[\frac{1 - q_m^{-\beta-2}}{1 - q_m^{-\beta-3}} \frac{\beta + 3}{\beta + 2} - 1 \right], \quad (11)$$

where I_H is the ionization potential. We use $\beta = 0$ and $q_m = 4$ for both H I and He II, which adequately approximates the shape of the spectrum found in numerical calculations when the emitted spectrum is a quasar power-law (with $\beta = 1.5$), and the effect of absorption by Lyman limit systems is taken into account (Miralda-Escudé & Ostriker 1990; Haardt & Madau 1996). This yields $\langle E_H \rangle = 0.43 I_H$ and $\langle E_{He} \rangle = 0.43 I_{He}$. We then obtain: $T'_H = 0.67$, and $T'_{He} = 1.11$. The total heating therefore falls short to compensate for cooling by a factor ~ 1.6 .

An obvious way to increase the heating rate is to assume that the He II reionization is not yet complete; in other words, that there are patches of low-density gas in the IGM where all the helium is in the form of He II. As discussed in Miralda-Escudé & Rees (1994), there are two reasons why the heating rate is higher during the reionization, relative to the case of photoionization equilibrium.

The first is that the ionization rate needs to be higher simply because every He II ion needs to be ionized once during the course of the He II reionization. The second is that *all* the hard photons will now be absorbed by a random He II ion in the IGM, up to the frequency $\nu_m = q_m \nu_0$ where the mean-free-path through the He II IGM reaches the horizon length. For the baryon density we use and at $z = 3$, and assuming also that about 50% of all the helium is in the form of He II in the diffuse IGM (and not in dense clouds having a small covering factor over the Hubble length), this maximum frequency is given by $q_m = 13$, i.e., a frequency 13 times higher than the He II ionization edge. The mean energy of the absorbed photons is therefore equal to the mean energy of the emitted photons up to this maximum frequency, *without* weighting them with the photoionization cross section:

$$\langle E_{He,r} \rangle = I_{He} \left[\frac{1 - q_m^{-\beta'+1}}{1 - q_m^{-\beta'}} \frac{\beta'}{\beta' - 1} - 1 \right], \quad (12)$$

where the subscript r in $\langle E_{He,r} \rangle$ indicates the mean energy per absorption during reionization, and the emitted spectrum from sources is $J_\nu \propto \nu^{-\beta'}$. For $q_m = 13$ and $\beta' = 1.5$, we obtain $\langle E_{He,r} \rangle = 0.71 I_{He}$. Since the recombination rate for He II at the mean density is equal to 1.6 times the Hubble rate H^{-1} at $z = 3$, and if the reionization is occurring over \sim a Hubble time near $z \sim 3$, it is reasonable to expect that the additional heating rate due to He II reionization is comparable to the heating rate due to balancing recombinations of He II. We therefore conclude that the heating from He II reionization can reasonably account for the IGM temperature we have determined here.

7.2. Usefulness for Measuring the Baryon Density from the Lyman Alpha Forest

One of the applications that the development of the new theory of the Ly α forest based on structure formation has had is to provide a measurement of the baryon density through its effect on the mean transmitted flux. For a fixed distribution of temperature, over-density, and peculiar velocities in the IGM, the Ly α optical depth at any point in the spectrum is proportional to $(\Omega_B h^2)^2 H(z)^{-1} \Gamma_{-12}^{-1}$, where $\Gamma = 10^{-12} \Gamma_{-12} \text{ s}^{-1}$ is the photoionization rate due to the cosmic ionizing background. To be specific, we define the parameter

$$\omega_B \equiv \Omega_B h^2 \left[\left(\frac{\Omega_0 h^2}{0.3 \times 0.65^2} \right)^{1/2} \Gamma_{-12} \right]^{-1/2}, \quad (13)$$

[where we have used $H(z) \simeq H_0(1+z)^{3/2} \Omega_0^{1/2}$, which is highly accurate at the relevant redshifts and in a flat universe]. As discussed by Hernquist et al. (1996), Miralda-Escudé et al. (1996), Rauch et al. (1997), Weinberg et al. (1997), and Paper I, a measurement of ω_B can be translated into a lower bound on $\Omega_b h^2$ by using the contribution to the ionizing background from known quasars as a lower bound on Γ_{-12} . This lower limit is on the high side of the range of Ω_b that is allowed by primordial nucleosynthesis: $\Omega_b h^2 \gtrsim 0.02$ (Rauch et al. 1997; Paper I).

One of the main model uncertainties in deriving the relationship between the parameter ω_B and the predicted mean transmitted flux is the mean IGM temperature. A higher temperature implies a lower recombination coefficient, and therefore a lower neutral hydrogen density. This implies that in order to reproduce a given observed mean transmitted flux, the mean density Ω_B needs to be increased further to compensate the reduced recombination coefficient. The measurements of the IGM temperature reported here and in Schaye et al. (2000), and Ricotti et al. (2000), all coincide in finding temperatures that are high compared to what is expected if the IGM is heated by photoionization and is in ionization equilibrium. As we have discussed, these higher temperatures can probably be understood as a result of the He II reionization. independently of its cause, the higher temperature implies an even higher value of ω_B than was obtained previously, which we can easily determine by modifying the temperature in the simulation to match the observations, as described earlier in §5.3. We find that, when the temperature in the simulation is increased to match the observed one, the derived value of ω_B is increased slightly to $\omega_B = (0.0336 \pm 0.0020, 0.0288 \pm 0.0023, 0.0248 \pm 0.0017)$ at $\bar{z} = (3.9, 3.0, 2.4)$, from the previous values $(0.0329, 0.0274, 0.0245)$ when the temperatures in the simulations are not modified (Paper I). The errors are derived from the observational errors in the determination of the mean flux decrement from Paper I.

Changing the temperature of the simulation affects the value of ω_B not only by modifying the recombination coefficient, but by increasing the amount of thermal broadening, which can spread the absorption in saturated regions to the outskirts of absorption lines, increasing the mean absorption for a given ω_B . We find that the effect of thermal broadening is less important than the effect of the reduced recombination coefficient. As an example, if we replace $\alpha(T) \rightarrow \alpha(T + 3000K)$ in every pixel in the simulation, the inferred ω_B increases by 0.0017 (where $\alpha(T)$ is the recombination coefficient), while the replacement $\sigma_b(T) \rightarrow \sigma_b(T + 3000K)$ changes ω_B by -0.00046 (where $\sigma_b(T)$ is the dispersion of the Gaussian thermal broadening). Dynamical effects caused by the increased pressure of the gas would probably go in the same direction as the thermal broadening, since they would tend to spread the gas in absorption systems over wider regions. However, it seems unlikely that any such dynamical effects (which can only be investigated by running the same simulation with different temperatures) can be more important than the thermal broadening effect. The examples shown in Theuns et al. (1999b) (see their Figure 6) appear to confirm that the dynamical effects of increased pressure are not more important than the increased thermal broadening when the gas temperature is raised.

With the statistical error bars we have obtained on the $T - \Delta_g$ relation, we can place more conservative lower bounds on ω_B than the ones obtained in Paper I. The lowest allowed value of ω_B needed to account for a given observed mean transmitted flux is obtained when T_\star is minimum and $\gamma - 1$ is maximum in equation (1), because that yields the minimum temperature for the low-density gas that determines the optical depth in unsaturated regions of the Ly α spectrum. We set T_\star equal to the measured value minus twice the statistical error bar given in Table 5, and $\gamma - 1 = 0.6$, which is the value valid when the IGM has been in photoionization equilibrium for a long time (Hui & Gnedin 1997). Any uniform heating of the IGM, such as that caused by reionization, should give

rise to a lower $\gamma - 1$, although shock-heating can increase $\gamma - 1$ above 0.6, the simulations show that this happens only at high enough gas densities that the Ly α absorption is already saturated. The error in our observational determination of $\gamma - 1$ is too large to give us a better constraint than $\gamma < 0.6$ (see Table 5).

The results of this exercise are $\omega_B > (0.0270, 0.0192, 0.0209)$ for $\bar{z} = (3.9, 3.0, 2.4)$, at 95% confidence, including the error from the mean flux decrement and the temperature measurements (added in quadrature). Using the lower bound obtained in Rauch et al. (1997) of $\Gamma-12 > 0.7$ in the range $2 < z < 3$, obtained by counting only radiation from the observed quasars, and not including the power-law extrapolation of the quasar luminosity function that has been observed only at redshifts $z < 2$, we obtain $\Omega_B h^2 > 0.017$. This result is still consistent with the determinations of the deuterium abundance (Burles & Tytler 1998). However, if the quasar luminosity function extends to low luminosities with a similar power-law slope as observed at $z < 2$, or if emission from galaxies increases significantly the intensity of the ionizing background, then the higher baryon density implied would come into conflict with the primordial nucleosynthesis predictions and the observed deuterium abundance.

In summary, we have reached the following conclusions:

1. The temperature of the IGM is $\sim 20000 \pm 2000\text{K}$ at density 1.4 times the mean, independent of redshift, although an increase of $\sim 3500\text{K}$ from $z = 3.9$ to $z = 3.0$ cannot be ruled out.
2. The high temperature cannot be explained by heating in ionization equilibrium, and probably indicates on-going He II reionization.
3. The contribution of temperature uncertainty to the uncertainty in the baryon density required by the observed mean flux decrement in the Ly α forest is now well constrained.

We thank Adam Steed and David Weinberg for helpful comments on the manuscript.

A. THE PROFILE FITTER

This algorithm has three input parameters that control how the fitting proceeds: E_d sets the amount that the flux must increase from the center point to the edges of the window before a fit will be attempted, W_{min} sets the minimum size of the window within which a fit is performed, and P_0 sets the quality of fit that will be accepted. In this paper we set $W_{min} = 2$.

Three more input parameters effect the speed of the code but are not important to the results: E_s controls the degree of symmetry around a central pixel that is required for a fit to be attempted, E_c sets the level of flux decrease, from the center pixel to the window edges, at which a point will be eliminated from consideration for fitting, and W_{max} sets the maximum allowed window size. These parameters are set to values large enough that they do not actually eliminate any profiles that would otherwise be accepted.

Before we describe the algorithm in detail, a few more terms must be introduced: We are going

to fit pieces of the spectrum that have center point P and extend $\pm W$ pixels to either side of P . The width of the fitting window, W , will be adjustable but constrained to $W_{min} \leq W \leq W_{max}$. The transmitted flux at a point P is $F(P)$. The error in the sum or difference of the flux at two points P_1 and P_2 is $\sigma(P_1, P_2) = [\sigma(P_1)^2 + \sigma(P_2)^2]^{1/2}$, where $\sigma(P)$ is the observational error in the flux at point P . The minimum acceptable probability for χ^2 is P_0 (we need to define P_0 by the probability because there will be varying numbers of degrees of freedom in the fits).

For a given spectrum the algorithm that we use is the following (the reader should keep in mind that, except for the added complication of setting the window position and width, this procedure just fits a single Voigt profile to each absorption maximum by χ^2 minimization):

1. Scan along the spectrum pixel by pixel searching for places where $|F(P - W_{min}) - F(P + W_{min})| < E_s \sigma(P + W_{min}, P - W_{min})$. Also require that $F(P) - F(P \pm W_{min}) < E_c \sigma(P, P \pm W_{min})$, where the flux at the $\pm W_{min}$ points is averaged. These places are candidates for a symmetric, non-concave profile.
2. If there is a significant increase in flux at the edges of the window, so that $F(P) - F(P \pm W_{min}) > E_d \sigma(P, P \pm W_{min})$, go ahead and fit Equation (4) to the absorption. If there isn't a significant increase try to expand the window.
3. To expand the window require that symmetry is maintained when W is increased, i.e., $|F(P - W) - F(P + W)| < E_s \sigma(P + W, P - W)$. If the window can be expanded return to step 2 to check if a fit can be done with the enlarged window, i.e., if $F(P) - F(P \pm W) > E_d \sigma(P, P \pm W)$.
4. If the region can't be fit, but also can't be expanded, eliminate the candidate point. Also eliminate the point if the window size has been increased to W_{max} without meeting the requirement for fitting.
5. Set initial parameters for the fit using $F(P)$ to set τ_c and $[F(P + W) + F(P - W)]/2$ to set σ_b . Set $v_c = 0$. If $F(P) < 0$ set $\tau_c = 10$.
6. Minimize χ^2 using the flux values and their error bars in the range of points between $P + W$ and $P - W$. Require that $|v_c| < 0.5$ pixels (outside this range is covered by other candidate points).
7. Eliminate candidate if $P(> \chi^2, \nu) < P_0$.
8. If P falls within W of a previously accepted candidate, eliminate the candidate with a smaller value of $P(> \chi^2, \nu)$. This does not eliminate any independent profiles because a single Gaussian would not fit if the window contained multiple lines.

REFERENCES

- Abel, T. & Haehnelt, M. G. 1999, ApJ, 520, L13
- Black, J. H. 1981, MNRAS, 197, 553
- Bryan, G. L., & Machacek, M. E. 2000, ApJ, 534, 57
- Bryan, G. L., Machacek, M., Anninos, P., & Norman, M. L. 1999, ApJ, 517, 13

- Burles, S. & Tytler, D. 1998, *ApJ*, 507, 732
- Cen, R., Miralda-Escudé, J., Ostriker, J. P., & Rauch, M. 1994, *ApJ*, 437, L9
- Croft, R. A. C., Hu, W., & Davé, R. 1999, *Phys. Rev. Lett.*, 83, 1092
- Croft, R. A. C., Weinberg, D. H., Katz, N., & Hernquist, L. 1998, *ApJ*, 495, 44
- Croft, R. A. C., Weinberg, D. H., Pettini, M., Hernquist, L., & Katz, N. 1999, *ApJ*, 520, 1
- Crotts, A. P. S., & Fang, Y. 1998, *ApJ*, 502, 16
- Gnedin, N. Y. 2000, *ApJ*, in press (astro-ph/9909383)
- Haardt, F., & Madau, P. 1996, *ApJ*, 461, 20
- Haehnelt, M. G. & Steinmetz, M. 1998, *MNRAS*, 298, L21
- Hernquist, L., Katz, N., Weinberg, D. H., & Miralda-Escudé, J. 1996, *ApJ*, 457, L51
- Hui, L. 1999, *ApJ*, 516, 519
- Hui, L., & Gnedin, N. Y. 1997, *MNRAS*, 292, 27
- Hui, L., Stebbins, A., & Burles, S. 1999, *ApJ*, 511, L5
- Madau, P. & Efstathiou, G. 1999, *ApJ*, 517, L9
- McDonald, P., & Miralda-Escudé, J. 1999a, *ApJ*, 518, 24
- McDonald, P., Miralda-Escudé, J., Rauch, M., Sargent, W. L. W., Barlow, T. A., Cen, R., & Ostriker, J. P. 1999, *ApJ*, submitted (astro-ph/9911196)
- Miralda-Escudé, J., Cen, R., Ostriker, J. P., & Rauch, M. 1996, *ApJ*, 471, 582
- Miralda-Escudé, J., & Rees, M. J. 1990, *ApJ*, 350, 1
- Miralda-Escudé, J., & Rees, M. J. 1994, *MNRAS*, 266, 343
- Nath, B. B., Sethi, S. K., & Shchekinov, Y. 1999, *MNRAS*, 303, 1
- Nusser, A. & Haehnelt, M. 2000, *MNRAS*, 313, 364
- Press, W., Teukolsky, S., Vetterling, W., & Flannery, B. 1992, *Numerical Recipes in C* (2d ed.; Cambridge:Cambridge University Press)
- Rauch, M., Miralda-Escudé, J., Sargent, W. L. W., Barlow, T. A., Weinberg, D. H., Hernquist, L., Katz, N., Cen, R., & Ostriker, J. P. 1997, *ApJ*, 489, 7
- Ricotti, M., Gnedin, N. Y., & Shull, J. M. 2000, *ApJ*, 534, 41

Schaye, J., Theuns, T., Rauch, M., Efstathiou, G., & Sargent, W. L. W. 2000, MNRAS, submitted (astro-ph/9912432)

Schaye, J., Theuns, T., Leonard, A., Efstathiou, G. 1999, MNRAS, 310, 57

Theuns, T., Leonard, A., Efstathiou, G., Pearce, F. R., & Thomas, P. A. 1998, MNRAS, 301, 478

Theuns, T., Leonard, A., Schaye, J., & Efstathiou, G. 1999, MNRAS, 303, L58

Theuns, T., Schaye, J., & Haehnelt, M. G. 1999, MNRAS, submitted (astro-ph/9908288)

Weinberg, D. H., Croft, R. A. C., Hernquist, L., Katz, N., & Pettini, M. 1999, ApJ, 522, 563

Weinberg, D. H., Miralda-Escudé, J., Hernquist, L., & Katz, N. 1997, ApJ, 490, 564

Table 1. Power-law fits to the $T - \Delta_g$ relation .

z	T_0 (K)	$\gamma - 1$ (for T)	\tilde{T}_0 (K)	$\gamma - 1$ (for \tilde{T})
4	14024	0.21	13873	0.22
3	15843	0.30	15584	0.30
2	12764	0.57	12954	0.54

Note. — \tilde{T} is the optical-depth-weighted average temperature at points in spectra (fitted vs. the density similarly averaged).

Table 2.

Setting	N_g	N_b	Q
$E_d = 25$	198	3	13.8
$E_d = 20$	236	11	14.3
$E_d = 17$	248	19	14.1
$E_c = 15$	264	22	14.3
$E_c = 14$	272	28	14.1
$E_c = 13$	271	34	13.6
$E_d = 12$	281	40	13.5
$E_d = 11$	285	56	12.4
$E_d = 8$	364	95	12.6
$E_d = 7$	386	137	10.9
$E_d = 5$	474	263	7.8
$E_d = 12$ (0.001)	284	41	13.5
$E_d = 12$ (0.1)	243	35	12.5
$E_d = 12$ (nn)	236	1	15.3
$E_d = 12$ (nc)	262	38	12.9
$E_d = 12$ (nr)	286	39	13.7
$E_d = 12$ (nr)	306	30	15.1
$E_d = 12$ (nr)	308	35	14.7

Note. — The quality measure $Q = (N_g - N_b)(N_g + N_b)^{-1/2}$, where N_g is the number of fitted features satisfying $0 \text{ K} < B - T < 3000 \text{ K}$ and N_b is the number satisfying $-3000 \text{ K} < B - T < 0 \text{ K}$. Entries labeled (0.1) and (0.001) have $P(> \chi^2) > 0.1$ and 0.001, respectively [the rest have $P(> \chi^2) > 0.01$]. The label (nn) means no noise, (nc) means no continuum fitting approximation, and (nr) means a new set of random numbers was used for the added noise in each example.

Table 3. Basic statistics of the observational data in each redshift bin.

z_{min}	z_{max}	\bar{z}	\bar{F}	\bar{n}	pixels	path length (km s^{-1})	E_d	absorption lines	τ_{min}	τ_{max}	lines used
3.39	4.43	3.89	0.48	0.029	35120	70893	8	281	3.8	47	98
2.67	3.39	2.99	0.68	0.011	35283	87308	12	284	1.0	19	160
2.09	2.67	2.41	0.81	0.028	36150	104581	9	223	0.41	5.4	179

Note. — The minimum (maximum) optical depth of fitted lines used in the temperature measurement is given by τ_{min} (τ_{max}). The mean noise level in the spectra is \bar{n} .

Table 4. Binned Results of Temperature from Observations

$\tau_{c,med}$	$\tau_{c,min}$	B_C (K)	ΔT (K)	Δ_g
$\bar{z} = 3.9$				
0.72	0.19	28200 ± 16700	16900	0.48
1.53	1.25	17400 ± 11200	11100	0.67
3.22	2.34	21200 ± 4100	6100	0.97
7.83	5.97	22400 ± 7900	3100	1.66
$\bar{z} = 3.0$				
0.43	0.18	25800 ± 2200	13800	0.61
1.03	0.62	24600 ± 3700	4400	0.90
1.55	1.29	21800 ± 2100	3000	1.15
4.80	2.93	25600 ± 5600	1600	2.53
$\bar{z} = 2.4$				
0.52	0.18	22600 ± 2600	2300	0.99
0.96	0.74	23200 ± 8500	3000	1.44
1.59	1.48	33000 ± 5400	1000	2.07
3.88	3.18	41600 ± 12100	-700	4.01

Note. — The temperature cutoff B_C , systematic offset ΔT , and gas density Δ_g , are given for each bin with minimum optical depth $\tau_{c,min}$ and median optical depth $\tau_{c,med}$.

Table 5. Power-law fits to Temperature from Observations.

\bar{z}_{obs}	z_{sim}	T_{\star} (K)	$T_{1.4}$ (K)	$\gamma - 1$	Δ_{\star}	T_0 (K)	τ_{\star}
3.89	4	20200 ± 2700	20100 ± 2800	0.43 ± 0.45	1.42 ± 0.08	17400 ± 3900	6.54
2.99	4	20200 ± 1300	20300 ± 1400	0.29 ± 0.30	1.37 ± 0.11	18400 ± 2100	1.83
2.99	3	19600 ± 1500	20400 ± 1800	0.33 ± 0.28	1.24 ± 0.10	18300 ± 1800	1.74
2.41	3	22600 ± 1900	20700 ± 1900	0.52 ± 0.14	1.66 ± 0.11	17400 ± 1900	1.07
2.41	2	23400 ± 2000	22800 ± 2100	0.51 ± 0.14	1.47 ± 0.10	19200 ± 2000	0.98